JGR Atmospheres

RESEARCH ARTICLE
10.1029/2022JD036920

Special Section:
Fire in the Earth System

Pyroconvection Classification Based on Atmospheric Vertical Profiling Correlation With Extreme Fire Spread Observations

Marc Castellnou[1,2,3], Mercedes Bachfischer[1,2], Marta Miralles[1,2], Borja Ruiz[1,2], Cathelijne R. Stoof[4], and Jordi Vilà-Guerau de Arellano[3]

[1]Catalan Fire & Rescue Service, Bombers GRAF, Barcelona, Spain, [2]FAST, Forest Fire Assessment and Advisory Team, European Union Civil Protection Mechanism Capacity, Madrid, Spain, [3]Meteorology and Air Quality Section, Wageningen University, Wageningen, The Netherlands, [4]Soil Geography and Landscape Group, Wageningen University, Wageningen, The Netherlands

Abstract Pyrocumulus (pyroCu) formation during convective fire-atmosphere interaction is a driving factor causing extreme and unpredictable wildfires. Here, by investigating several cases of pyroCu occurrence, we have monitored fire-induced changes in atmospheric boundary layer (ABL) vertical profiles of state variables (temperature, humidity, and wind). Particular emphasis is placed in relating them to observed versus modeled fire spread biases. To this end, during the 2021 fire season in the Iberian Peninsula, we conducted a pyroconvection monitoring campaign. We gathered data on hourly fire spread, plume surface, deepening and penetration stages, and in-situ radiosoundings within wildfire plumes. European Centre for Medium-Range Weather Forecasts ERA5 weather data completed the analysis as reference modeling information to characterize the meso and synoptic scales on the thermodynamic profiles. We propose a novel classification of pyroconvection-type events based on (a) differences in ABL thermodynamic stability, (b) regions characterized by high turbulence in the sub or pyroCu-layers, and (c) the reinforced entrainment of free-tropospheric air on top of every convective plume. This classification defines four types: (a) convective plumes, (b) overshooting pyroCu, (c) resilient pyroCu, and (d) deep pyroCu/pyroCb. Those prototypes change ABL conditions (temperature, humidity, height) differently depending on the dry or moist convection enhancement that drives them. Using this distinct behavior, we find correlations between observed ABL thermodynamic changes after fire-atmosphere interaction and fire spread biases. Our findings pave the way to quantify the pyroconvection effect on fire spread and facilitate safer and more physically sound decisions when analyzing extreme fires.

Plain Language Summary Extreme wildfires pose severe problems for responders and managers. Those fires are unpredictable, driven by fire-induced convection phenomena such as pyrocumulus (pyroCu). Therefore, to anticipate fire spread in these uncertain scenarios, we need to understand pyroCu formation better. During the 2021 summer season in Iberian Peninsula, we monitored pyroCu events and launched sondes into the fire plumes. To investigate fire-induced changes in atmosphere vertical profile variables (temperature, humidity, and wind), we compared these in-situ sonde measures with modeled profiles from atmospheric model ERA5. Finally, we correlated the atmospheric vertical profile changes with fire spread biases. We identified different types of changes characterized by four distinctive types of pyroclouds. In all cases, changes resulted from air mass dryness from the upper layers of the atmosphere being transported down into the lower layers. The resulting modified atmospheric boundary layer created different than expected burning conditions and changed fire behavior to the extreme. We quantified those changes in fire rate of spread correlated with the updraft vertical velocity inside the fire plume. This research proposes a first quantitative correlation to predict extreme wildfire behavior driven by pyroCu.

Key Points:

- Importance of turbulence near the atmospheric boundary layer (ABL) entrainment zone to determine the classification of pyroconvection types
- Pyrocloud layer entrainment into sub-pyrocloud layer creates moist or dry convection regimes, defining the changes induced into ABL
- The fire plume updraft vertical velocity is positively correlated to fire rate of spread bias during pyroconvection events

Supporting Information:

Supporting Information may be found in the online version of this article.

Correspondence to:

M. Castellnou,
mcastellnou@gencat.cat

Citation:

Castellnou, M., Bachfischer, M., Miralles, M., Ruiz, B., Stoof, C. R., & Vilà-Guerau de Arellano, J. (2022). Pyroconvection classification based on atmospheric vertical profiling correlation with extreme fire spread observations. *Journal of Geophysical Research: Atmospheres*, *127*, e2022JD036920. https://doi.org/10.1029/2022JD036920

Received 10 APR 2022
Accepted 1 NOV 2022

Author Contributions:

Conceptualization: Marc Castellnou, Cathelijne R. Stoof, Jordi Vilà-Guerau de Arellano
Data curation: Marc Castellnou, Mercedes Bachfischer, Marta Miralles
Formal analysis: Marc Castellnou, Mercedes Bachfischer, Marta Miralles
Investigation: Marc Castellnou, Borja Ruiz

1. Introduction

High fireline intensities can trigger fire-atmosphere interaction, producing more extreme and often unexpected fire behavior. These fire-line intensities have been enhanced in recent decades by the increase in fuel load (Di Virgilio et al., 2019; Ruffault et al., 2018; Turco et al., 2018) after changes in landscape management (Pyne, 2019) and by climate change-driven aridity (Abatzoglou et al., 2019). The resulting extreme wildfires are overwhelming fire service operational capacity and becoming a new normal (Jolly et al., 2015), even with reinforced efforts and advanced technologies. The increase in extreme wildfires has had an impact on a global scale, resulting in dramatic consequences in terms of human lives: 173 deaths in Australia in 2009; 110 deaths between June and

Methodology: Marc Castellnou, Mercedes Bachfischer
Resources: Marc Castellnou
Software: Marc Castellnou, Mercedes Bachfischer
Supervision: Jordi Vilà-Guerau de Arellano
Validation: Marc Castellnou, Mercedes Bachfischer
Writing – original draft: Marc Castellnou
Writing – review & editing: Marc Castellnou, Mercedes Bachfischer, Marta Miralles, Borja Ruiz, Cathelijne R. Stoof, Jordi Vilà-Guerau de Arellano

October 2017 in wildfires in Portugal; 102 deaths in Kineta, Greece, in 2018; 85 deaths in Santa Rosa, California, in 2017; 94 deaths in Paradise, California, in 2018. As such, there is a critical need to understand fire-atmosphere interactions better to predict and manage extreme fires.

What defines these extreme fire types is the bias between modeled and observed fire behavior (Rothermel, 1991). Such bias has previously been used to assess fire-atmosphere interaction's impact during pyroconvective formation (Andrews et al., 2011). During those events, pyrocumulus and pyrocumulonimbus (pyroCu and pyroCb) (AMS, 2021) have emerged as the maximum pyroconvective element of extreme fire-atmosphere interaction, creating unpredictable fire behavior (Fromm et al., 2010; Goens & Andrews, 1998; Lareau & Clements, 2016). However, it was not until the 2003 and 2009 Australian firestorm events (McRae, 2003) that the importance of pyroCu/Cb on the "new normal" extreme fire was identified. These first events have been confirmed as a worldwide trend linked to more frequent episodes of drought and climate change-associated heat waves (Duane et al., 2021). Representative examples are Chile 2017 (EUCPM, 2017), Portugal 2017 (Guerreiro et al., 2017, 2018), California 2018 (Lareau et al., 2018), Australia 2019/2020, and California 2020 and 2021.

PyroCu/Cb effects on fire behavior have been reported to enhance the fire intensity and the rate of spread (ROS) (Fromm et al., 2010). However, although fire behavior change to the extreme is a known consequence of pyroCu/Cb formation, the measurable relationship between the thermodynamic characteristics of pyroCu and the fire behavior change is still not defined. In that sense, atmospheric boundary layer (ABL) thermodynamic characterization is used to assess PyroCu occurrence during fire events. Qualitative and quantitative indicators based on atmospheric vertical profile models are used to anticipate pyroCu occurrence and warn of sudden changes in fire spread.

The first attempts to classify types of extreme fire spread differentiated wind-driven and plume-dominated wildfires. These relationships were based on the power of the fire versus the power of the wind ratio (Byram, 1959), later named convective number (Nc) (Nelson, 1993). In short, Nc quantifies the ratio between buoyant and shear-driven turbulence on the atmospheric vertical profile. However, a shortcoming is that the Nc value, although used to assess the potential changes from the wind to the plume-driven type or vice versa (Guerreiro et al., 2017; Morvan & Frangieh, 2018; Werth et al., 2016), is inadequate as a metric of measurable change on ROS, flame length or spotting distance (Finney et al., 2021).

Further analysis to quantify fire-atmosphere interactions includes vertical profile modeling analysis to determine how ABL stratification and stability relate to fire behavior. The process is broadly used to assess the chances for the plume to reach lifting condensation level (LCL) or convective condensation level (CCL) and the likelihood of pyroconvection phenomena (Charney & Potter, 2017; Tory et al., 2018). The most common vertical profile producing pyroCu/Cb formation (Goens & Andrews, 1998; Johnson et al., 2014; Lareau & Clements, 2016; Peterson et al., 2015, 2017) is identified as a well-mixed dry ABL with a moist layer on top. In a SkewT diagram, a classic inverted-V shape can identify these conditions (Beebe, 1955; Wakimoto, 1985). The physical interpretation is connected to two different stages within the pyroconvective process: (a) indraft caused by the sudden fire plume growth when reaching free convection level and (b) downdraft with gusty and erratic winds following pyroCb maturity, leading to an erratic expansion of the fire (Potter & Hernandez, 2017).

Meteorological indices are commonly used to assess the likelihood and strength of this process's concatenation. For example, the Haines Index (Haines, 1988) is computed by θ (K) differences between two heights on the fire atmosphere's vertical profile, assessing its instability. It has been successfully used to predict extreme fires but has not been performing well in recent events. It has been observed not to be sensitive enough for decision-making between fire days, since it tends to build up to its maximum value without allowing the differentiation of fire days (Pinto et al., 2020; San-Miguel-Ayanz et al., 2020). Convective available potential energy (CAPE), used in meteorology to forecast storms, has also been used for fire connectivity assessment (Moncrieff & Miller, 1976). As a complement, downdraft convective available potential energy, or downward CAPE, is also considered to capture the downdraft effects over fire spread (Potter & Hernandez, 2017). However, fire-induced CAPE, named fireCAPE by Potter (2005), needs to be computed, making assumptions on how much temperature or specific humidity will be added by the fire. Potter (2005) proposed a potential temperature and specific humidity perturbation of 2 K and 2 g kg^{-1}, but Luderer et al. (2009) adjusted it to 2 K and 0.2 g kg^{-1}. The pyrocumulus firepower temperature (PFT) approach by Tory et al. (2018), Tory and Kepert (2020) has recently provided a different method to eliminate the need for such assumptions. Instead, it proposes computing the minimum fire energy

release to trigger the pyroCb under the expected mixing layer conditions. Complementing the PFT concept, Leach and Gibson (2021) propose quantifying the potential for pyroconvection.

Nevertheless, all the above indices and measures still lack proper translation into fire behavior variables, such as the measurable increase in ROS (m s^{-1}), burnt area rate (ha·h^{-1}), or spotting distance (m). Leach and Gibson (2021) recognized this limitation in their work on the potential for pyroconvection.

The development of fire-atmosphere coupled models such as MESO-NH ForeFire (Filippi et al., 2009) and WRF-Fire (Kochanski et al., 2015) has helped to quantify fire behavior changes due to fire-atmosphere interaction. Their application has improved dramatically over the last 15 years. However, they are still limited in terms of the verifiable physical theory of fire spread (Finney et al., 2021) and the fire-atmosphere interactions under different types of pyroconvection events (Bakhshaii et al., 2020).

In fact, what is classified under pyroconvection includes different observed fire plumes and pyroCu types impacting differently on fire spread patterns. The different types of fire-atmosphere interaction have been previously described as different convective regimes, generally classified as "dry" and "moist" convection (Wakimoto, 1985). The moist regime has been identified as the one developing deep pyroCu/Cb and the most extreme fire behavior (Fromm et al., 2010). The transitions between those conditions are important and need better understanding since they develop sudden changes in fire spread. A representative example of pyroconvection dynamism is what occurred during the October 2017 extreme events in Portugal (Castellnou et al., 2018; Guerreiro et al., 2018). Using the classification we present here, three types of pyroconvection were observed. First, fires transitioned from surface layer plumes to pyroconvective plumes with overshooting pyroCu. The transition created sudden increases in the fire ROS. Second, the fires grew intense and their plume deepening above ABL allowed a transition from dry to moist convection, creating and maintaining a resilient pyroCu. The second transition created sudden changes in spread direction and further changes in ROS. Finally, after humidity advection driven by the arrival of a cold front into the area, plumes showed a third transition to deep moist convection creating a pyroCb, followed by chaotic downdraft-driven expanding fires.

The Portugal 2017 case shows a critical need for accurate data on how different types of pyroconvection affect the ABL thermodynamics, inducing a new fireABL that will imply changes in fire spread. The information needed can be collected by launching radiosondes directly into the fire plume or by radar Doppler readings of fire plumes (Lareau & Clements, 2016, 2017). The different processes can then be correlated with differentiated changes in fire spread.

Our main goal was to move forward and establish relationships between the development of different pyroconvection types and their impact on fire behavior change to be used in the operative field when making decisions. Therefore, with this study, we have aimed to identify different pyroconvection processes and relate them to measurable changes in fire spread variables. To separate pyroconvection, we have proposed a classification using the turbulence levels within the ABL, namely LCL, ABL and maximum wind shear height. Due to proposing this classification based on the data gathered in only one fire campaign, the different pyroconvection forms will be identified as "prototypes."

For our research, we launched 13 sondes in seven active fires with known fire spread characteristics during the 2021 fire season in the Iberian Peninsula.

2. Fundamental Concepts and Methodology

During the 2021 Iberian Peninsula fire season, we conducted a pyroconvection campaign to classify different PyroCu motions and their influence on fire spread changes during observed extreme fire behavior events. The methodology is organized first by describing the fundamental concepts used to characterize plumes, boundary layer thermodynamics, and fire spread (Section 2.1). Second, we describe the field methodology for launching sondes into the fire plume (Section 2.2). Third, we describe how biases between observed and modeled fire spread are identified as extreme fire events (Section 2.3). Fourth, we describe how we analyze the vertical profiles measured on the field campaign and frame them with the ERA5 model to characterize the fire-induced changes in the vertical profile (Section 2.4).

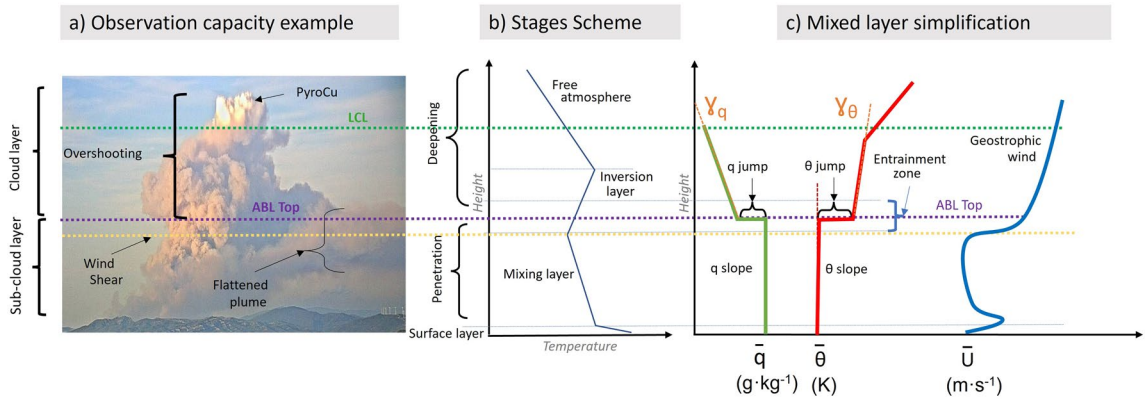

Figure 1. Plume characteristics observation scheme and equivalence with plume stages and mixed layer parametrization. (a) Observed plume characterization during Santa Coloma de Queralt fire on the 24 July 2021 (Table 1). Flattened plume, overshooting, and pyroCu are added to reinforce the characteristic needed to classify pyroconvection. (b) boundary-layer description including surface, penetration, and deepening stages (Potter, 2002). (c) Characterization of the atmospheric boundary layer (ABL) using mixed-layer theory (Stull, 1988). The dotted lines connecting the three figures are: estimated ABL top in violet, lifting condensation level in green, and wind shear in yellow.

2.1. Fundamental Concepts to Characterize Pyrocumulus and Its Relation to Surface Fire Spread

The fundamental concepts used in this study are based on (a) the classification of visible plume characteristics adapted to plume stages (Potter, 2002); (b) thermodynamics and state variables in the mixed-layer theory (Stull, 1988), and (c) fire behavior modeling as described by Andrews (2018).

2.1.1. Plume and ABL Characteristics

Directly observing the plume rising process into ABL provides the first data to classify pyroconvection events. Figure 1 conceptualizes the plume characteristics observed during the fire (Figure 1a), its equivalence with the ABL layers and plume stages (Figure 1b), and the ABL thermodynamic variables used by the mixed-layer theory scheme (Figure 1c). We describe below the main concepts used in this study:

ABL levels and ratios:

- *ABL top*: mixing layer height (m).
- *Maximum wind shear*: height (m) of the maximum wind gradient (m s^{-1}). Visible in the plume observations because it breaks and tilts the plume.
- *LCL*: height (m) at which a parcel of moist air lifted dry-adiabatically would become saturated.
- *LCL/ABL and shear/ABL height ratio*: a measure of the turbulence height above (>1) or below ABL (<1)

Although Lareau and Clements (2016, 2017) proposed CCL as a better metric to identify the pyroCb cloud base, we use LCL as a more generic variable. LCL enables us to group fire observations under all sorts of atmospheric conditions, following recent works assessing the potential of pyroCu formation (Leach & Gibson, 2021; Tory & Kepert, 2020; Tory et al., 2018).

When referring to the levels, we will differentiate between the environment and those inside the fire. Therefore, we will refer them inside the fire as **fireLCL**, **fireABL**, and **fireShear**.

Plume characteristics:

- *Flattened plume*: thick smoke stratified layer, without buoyancy.
- *Overshooting*: when the buoyant smoke plume rises momentaniously above the flattened plume top layer (Biondi et al., 2012; Dworak et al., 2012).
- *PyroCu*: a cloud formed by a rising thermal from a fire when it reaches LCL (American Meteorological Society, 2021).
- *PyroCb*: an extreme manifestation of a pyroCu when deepening above LCL and rising to the upper troposphere or lower stratosphere (American Meteorological Society, 2021).

Although The World Meteorological Organization defined in 2017 these types of clouds as flammagenitus clouds (WMO, 2017), the pyroCu and pyroCb definitions from the American Meteorological Society are used in this paper.

- *Plume updraft*: rising convective wind inside a smoke plume.
- *Plume indraft*: radial surface wind at smoke plume base induced by an updraft.

Observable plume characteristics are combined with the plume stages scheme, proposed by Potter (2002). Plume stages thermodynamically characterize the plume's rising (Figure 1b) through the ABL or above it:

- *Surface stage*: the plume grows inside the ABL surface layer, roughly estimated and assumed to be 10% of its total height (Troen & Mahrt, 1986).
- *Penetration stage*: the fire plume breaks into the ABL mixing layer. The induced indraft due to plume rising drives effects over the fire.
- *Deepening stage*: the plume breaks above ABL, entering the entrainment zone and deepening into the free tropospheric stable layer. The θ lapse rate will condition further vertical development.

If during penetration or deepening stages condensation occurs and a Pyrocloud is formed, we will then follow the mixed layer notation (Vilà-Guerau de Arellano et al., 2015) and incorporate:

- *Pyrocloud layer*: layer above the mixing layer where the cloud develops to the top of convection
- *Sub-pyrocloud layer*: well-mixed layer below the cloud.

2.1.2. Vertical Structure Characteristics

We subsequently compared plume characteristics and stages with the mixed layer theory, as in Vilà-Guerau de Arellano et al. (2015) (Figure 1c), as the first approach to estimate the thermodynamics involved in the plume rise through the ABL structure.

The intercomparison of fire and environmental observed vertical profiles with modeled profiles was done based on the conserved variables (Figure 1c): specific humidity (q) and potential temperature (θ). Their gradients on the mixing layer ($\partial\theta/\partial z$ and $\partial q/\partial z$, θ-gradient and q-gradient, respectively) are essential to determine ABL stability (Liu & Liang, 2010; Vogelezang & Holtslag, 1996). The jumps at the entrainment zone between ABL and free atmosphere (Δq, $\Delta\theta$) and lapse rates on the free atmosphere (γ_q, $\gamma\theta$) assess the ability of a parcel to penetrate above ABL and achieve free convection. The characterization is completed with the three components of wind (u, v, w), relative humidity (RH), ABL, LCL and shear height, and available CAPE.

The Bulk Richardson number ($\mathrm{Ri_b}$) represents a dimensionless number that compares convective versus mechanical turbulence. In our specific case, we define a critical Richardson number, that is, $\mathrm{Ri_{bc}} > 0.33$ (Zhang et al., 2014) to estimate the boundary-layer height. The preference for $\mathrm{Ri_b}$ is based on its higher reliability under variability of conditions (Richardson et al., 2013).

$$Ri_b = \frac{\left(\frac{g}{\theta_{v0}}\right)(\theta_{vh} - \theta_{v0})\,\mathrm{h}}{u_h^2 + v_h^2} \tag{1}$$

where g represents gravitational acceleration ($\mathrm{m\cdot s^{-2}}$), θ_{vh} and θ_{v0} are virtual potential temperatures (K) at level h (ABL height) and surface, and u_h and v_h are the wind speed ($\mathrm{m\cdot s^{-1}}$) at level h.

LCL was computed based on $\mathrm{LCL_S}$ (surface conditions) using an iterative approach, as in METPY library (May et al., 2022), consisting of computing dew point from LCL pressure and surface mixing ratio and LCL pressure from surface temperature and mixing ratio.

CAPE was computed using Fire-CAPE (Potter, 2005), which integrates the fire effect on modifying ABL surface layer:

$$\mathrm{FireCAPE} = g\int_0^z \frac{(\theta_{\mathrm{ev}}(0) + \Delta\theta_{\mathrm{f}}(0)) - (\theta_{\mathrm{ev}}(z') + \Delta\theta_{\mathrm{f}}(z'))}{\theta_{\mathrm{ev}}(z') + \theta_{\mathrm{f}}(z')}\mathrm{d}z \tag{2}$$

where θ_{ev} and θ_{f} (K) are read as potential temperature from the environment and fire, z (m.a.g.l.) is the elevation on the vertical profile, and g ($\mathrm{m\cdot s^{-2}}$) is the gravitational acceleration.

2.1.3. Fire Behavior Characteristics

A necessary aspect of our research was to correlate extreme changes in fire spread patterns with pyroconvection events occurrence. The extreme fire concept was considered following Werth et al. (2016). In their work, they identified extreme fires as those related to coupled fire-atmosphere dynamics. The predictability of fire spread during such extreme moments depends not only on surface conditions but also on the thermodynamic state variables and their vertical distribution in the atmosphere.

When characterizing and modeling fire spread, we were interested in the energy released within the ABL to quantify fire interaction with the atmosphere. Therefore, we considered the following variables:

- *ROS*, in $m \cdot s^{-1}$, defines the fire forward propagation speed over a landscape. We will consider the head fire ROS.
- *Burnt ratio* ($ha \cdot h^{-1}$): expresses the surface burnt per unit of time. Although it is $m^2 \cdot s^{-1}$, it is mainly used in $ha \cdot h^{-1}$.
- *Fireline intensity* (*FLI*), in $kW \cdot m^{-1}$, expresses the energy the fire is releasing per unit of the forward spreading front. It is the primary measure to calculate fire effects. We use the Byram (1959) definition:

$$\mathrm{FLI} = H * w * \mathrm{ROS}, \tag{3}$$

Where FLI is Byram's fireline intensity ($kW \cdot m^{-1}$), H is the heat yield of fuel involved ($kJ \cdot kg^{-1}$), w is the weight of the available fuel ($kg \cdot m^{-2}$) and ROS is the rate of forward spread ($m \cdot s^{-1}$).

Observed fire spread data were obtained from the FRS (fire and rescue service) following mapping of the observed fire perimeter position. We then computed the ROS using the maximum hourly distance traveled by the fire front between two consecutive isochrones and following wind direction.

Modeled ROS was obtained using Rothermel's (1972) semiempirical fire spread model, as described by Andrews, 2018. A landscape database (Finney, 1998) for each fire was needed to run the simulations. In that sense, topography was modeled using a 30 m resolution digital terrain model. The weather was obtained from an official automatic weather station network (Servei Català de Meteorologia, 2021). The fuel types were characterized according to Anderson fuel types (Anderson, 1982), extracted from lidar-based fuel layers (González-Olabarria et al., 2019) in PREVINCAT server (PREVINCAT, 2021). We followed the simulation methodology as in Finney (1998) and Andrews (2009).

Equation 3 was then used to estimate FLI with the modeled and real measured fire ROS.

2.2. Sounding Observations: Procedure and Evaluation

2.2.1. Launching Methodology

To compare the thermodynamic characteristics of the fire-modified atmosphere with the environment's vertical profile, we launched sondes inside the fire plume on days with pyroconvective favorable conditions (see Text S1 in Supporting Information S1). The launching position is key for the measurement, as illustrated in Figure 2. It requires special procedures (Figure 2a) and a position as close as possible to the convective plume and its indraft. We expected the sonde to be caught inside the lateral convective vortex (Finney et al., 2021) as drafted in Figure 2b. In doing so, we forced the sonde to be sucked directly into the plume developing above the head fire, to capture the intensive updraft inside the plume's core.

To ensure that the launching of sondes was carried out safely, several essential precautions were taken. First, fires can change behavior and rapidly increase ROS. Second, sondes launched near the fire front can present a risk to aircraft involved in fire management operations. Third, the launching process must be carried out quickly to prevent exposure to the risk of the launching team getting trapped in the fire. Consequently, we ensured careful coordination with the incident command and control to launch the sondes close to the plume.

2.2.2. Quality of Fire Sonde Type Compared With LIAISE Sonde

To ensure confidence in our observations, we evaluated the reliability of the light-sounding system used (see Table S1 in Supporting Information S1) during the campaign. The fire-sondes were calibrated with regular meteorological sondes Vaisala RS41-SG at the official LIAISE experiment (Boone et al., 2019), used by Météo-France on 10 July 2021. They were both launched in-situ and at the same time to compare accuracy. A satisfactory agreement

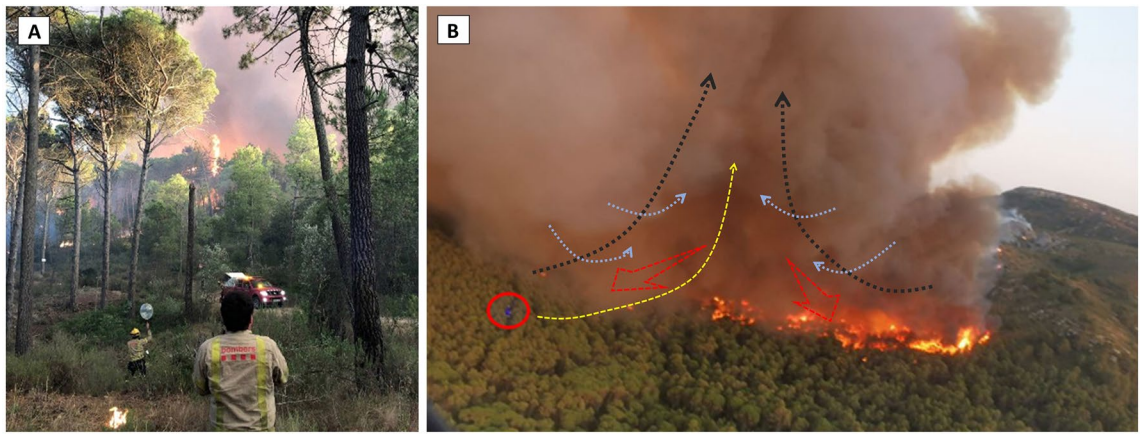

Figure 2. Launching sonde T21 (Table 1) at the head of Torroella fire (22 July 2021). (a) Launching site at the fire-head, approximately at 150 m downwind of the head-fire (see Text S1 in Supporting Information S1). Observe the spotting around the firefighters with the car ready to leave to the safety zone (See Movie S1). Vertical buoyant flames under the plume can be observed above the pines as a clear signal of plume-dominated environment. (b) The perspective of the launching moment (see Movie S2) with team position (red circle). The picture shows the fire spreading direction (red arrows) and the two counterrotating vortexes (blue arrows) created by the plume indraft on every flank when converging at the base of the head plume (black arrows). The yellow line shows the aimed sonde trajectory inside the plume (Picture source: Bomberscat).

between the temperature (T_s), dew point temperature (T_d), and wind bars (speed and direction) was observed on both sonde's profiles projected on a skew-T chart (Figure 3), coinciding with a similar experiment by Bessardon et al. (2019). The same layering was observed in terms of thermal inversion and wind shear, including the unstable ABL from surface to 910 hPa and the 3 K inversion and wind shear around 900 hPa.

2.3. Extreme Event Identification

In our research, we compared the modeled with the observed ROS ($m \cdot s^{-1}$) and FLI ($kW \cdot m^{-1}$). The bias of observed versus modeled ROS and FLI during pyroconvective events is then evaluated to quantify possible fire-atmosphere interaction effects. We have identified extreme events when the observed versus modeled ratio value equals or exceeds 3 (Rothermel, 1991).

Our fire behavior analysis is based on ROS and ROS is an observable measure of fire behavior used by fire services and is well estimated by surface spread models (Finney et al., 2015). It is a reliable variable to obtain FLI (Equation 3) and estimate the fire's heat flux or power (Harris et al., 2012) that the fire front is introducing into the ABL.

2.4. ABL Mixing Layer Thermodynamics Characterization for Pyroconvective Prototypes

To assess fire-induced changes in the thermodynamic profile, we compared our observations of plume-atmosphere interaction with vertical profiles from sondes (in and out of the fire) and modeled vertical profile data to cover the

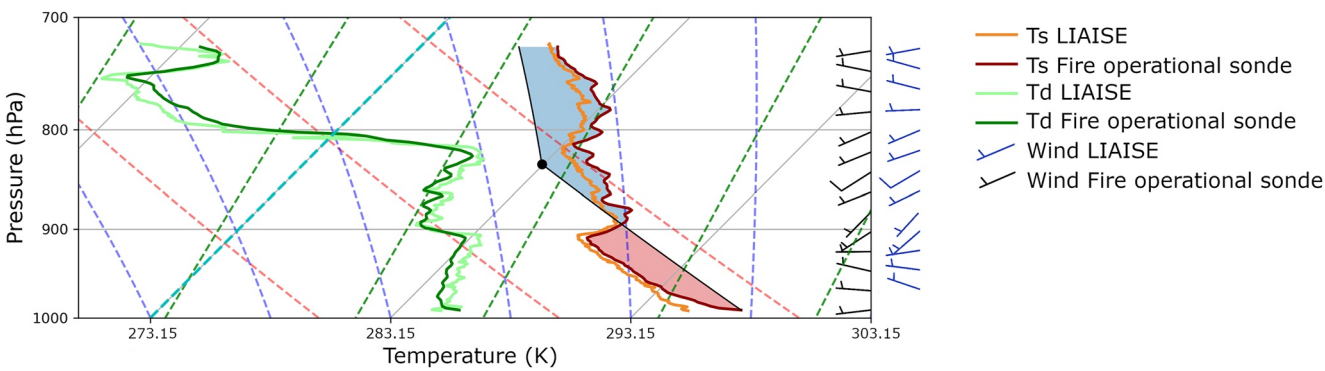

Figure 3. Comparison and calibration of the fire-operational sondes consisting of small storm balloons. Ambient temperature (T_s), dew point (T_d), and wind bars (direction and intensity) are shown for both sondes. LIAISE by MeteoFrance, and fire-sondes were launched at 13:30 UTC on the 10 July from the same spot at Ivars d'Urgell. As observed, the match with the two systems was satisfactory on all variables (pressure, T_s, T_d, wind speed, and wind direction).

daily ABL dynamics. For modeled data, we introduced the ERA5 data set (Hersbach et al., 2020) from European Centre for Medium-Range Weather Forecasts, with 0.25° spatial resolution computed every hour. The 37 original levels of the ERA5 output are interpolated to achieve a profile with data every 10 m and facilitate intercomparison with fire-sonde data.

We know that model results such as ERA5 cannot resolve atmospheric features driven by steep topography or sub-grid effects due to surface heterogeneities. However, the model adequately captures synoptic and meso-alpha patterns (Thunis et al., 2007) in which fire is evolving. Indeed, ERA5 is currently used by the fire community (Artés et al., 2022). Model results calculated using a higher resolution, that is, using for instance, AROME or WRF, could have been used, but this will be future research (Eghdami et al., 2021).

In Text S2 and Figure S1 in Supporting Information S1, we present the ERA5 validation compared with LIAISE and in-fire sondes.

2.4.1. Drafting Pyroconvection Prototypes

Fire plume interaction with ABL had been characterized following Section 2.1.1 to propose the first pyroconvection prototypes. The classification was based on ABL stability, plume characteristics (flattened, overshooting, PyroCu, PyroCb), plume stages (surface, penetration, or deepening), and turbulence position (height) on top of ABL. ABL stability is determined according to Liu and Liang (2010), as unstable (θ-gradient $< 0.10^{-3}$ K·m^{-1}), stable (θ-gradient $> 1.10^{-3}$ K·m^{-1}) or neutral ($0 < \theta$-gradient $< 1.10^{-3}$ K·m^{-1}). Turbulence position assessment was carried out using primary ratios: LCL/ABL height (m) and shear/ABL height (m). Values >1 or <1 point to turbulence above or below ABL.

2.4.2. Assessing Fire-Atmosphere Interaction-Induced Changes

The analysis is based on conserved meteorological variables (q, θ, Δq, $\Delta\theta$, γ_q, and $\gamma\theta$) as described in Figure 1c and Section 2.1.2. Relevant to our analysis is the calculation of critical variables: ABL and LCL height, maximum shear height (m), fireCAPE and plume updraft vertical speed. The plume updraft vertical speed is computed considering relative rising balloon ascent (m·s^{-1}) in our sondes.

We used the Richardson Ri_b (Equation 1) to compute ABL height. The recommended procedure (Zhang et al., 2014) proposes beginning to compute it at 200 m AGL to avoid surface layer disturbance on the ABL height estimation. However, we observed that the surface layer, where we launched the sonde to ensure it is entrained into the fire-thermal plume, is dominated by plume indraft winds converging at the plume base (Charland & Clements, 2013) as observed in Movie S3. Applying Rib methodologies without ruling this indraft surface layer out will show a significantly lower ABL according to wind shear and stability. Therefore, we propose to compute Rib starting above the surface layer, estimated to be roughly 400 m AGL.

We first compared the observed fire plume radiosondes with the environmental ones measured nearby but outside the fire. We focused on the θ, q, RH and vertical updraft speed to assess fire-induced changes on the vertical profile and prove fire causality.

Second, we focused on comparing the obtained vertical profiles inside the fire plume with the modeled ERA5 profiles. We completed for every singular in-fire sonde observation the comparison of θ, q, RH and updraft vertical speed as well as fireLCL and fireABL height with ERA 5 modeling expected ABL and LCL height. We focused our analysis on the pyroconvective event from Section 2.3, including previous and after-hours modeled profiles to frame the pyroconvective event properly.

3. Results

The results are presented first by classifying fire spread characteristics to identify the extreme fire behavior moments (Section 3.1). Second, we have described these identified extreme moments according to the initial ABL environmental conditions and observed plume characteristics (Section 3.2). Third, we have proposed pyroconvection prototypes for every extreme moment mentioned (Section 3.3). Fourth, for every pyrocovection prototype, we have analyzed the fire-atmosphere-induced changes in the vertical profile thermodynamics (Section 3.4). Finally, we have correlated the fireABL thermodynamic changes with fire spread biases identified to prove causality (Section 3.5).

We monitored 144 hr of fire-atmosphere interaction from seven fires during our 2021 campaign (Castellnou et al., 2022). Five fires have the complete data set, and two have observations but no sounding. In Figure 4, we show the location of each fire. In orange we signal those fires that showed a pyroconvective event, its plume was monitored, and sondes were launched into its fire plume. In yellow we signal the fires that a successful sonde couldn't reach the plume but were monitored. A total of 13 successful sondes were launched, capturing pyroconvective events during seven different wildfires. Horizontally, these fires varied in size from 60 to 7,400 ha, with a vertical plume height of 900–7,900 m. The fire perimeters in Figure 4 show the hourly isochrones with the overlaid sondes trajectories to better understand the fire spread pattern. Unfortunately, we had issues with the quality of data recovered on two of our fires with successful sondes. In Pobla Massaluca (Figure 4d), contact with sonde was lost before reaching the ABL top. In Sierra Bermeja (Figure 4e), we could not recover appropriate hourly spread data.

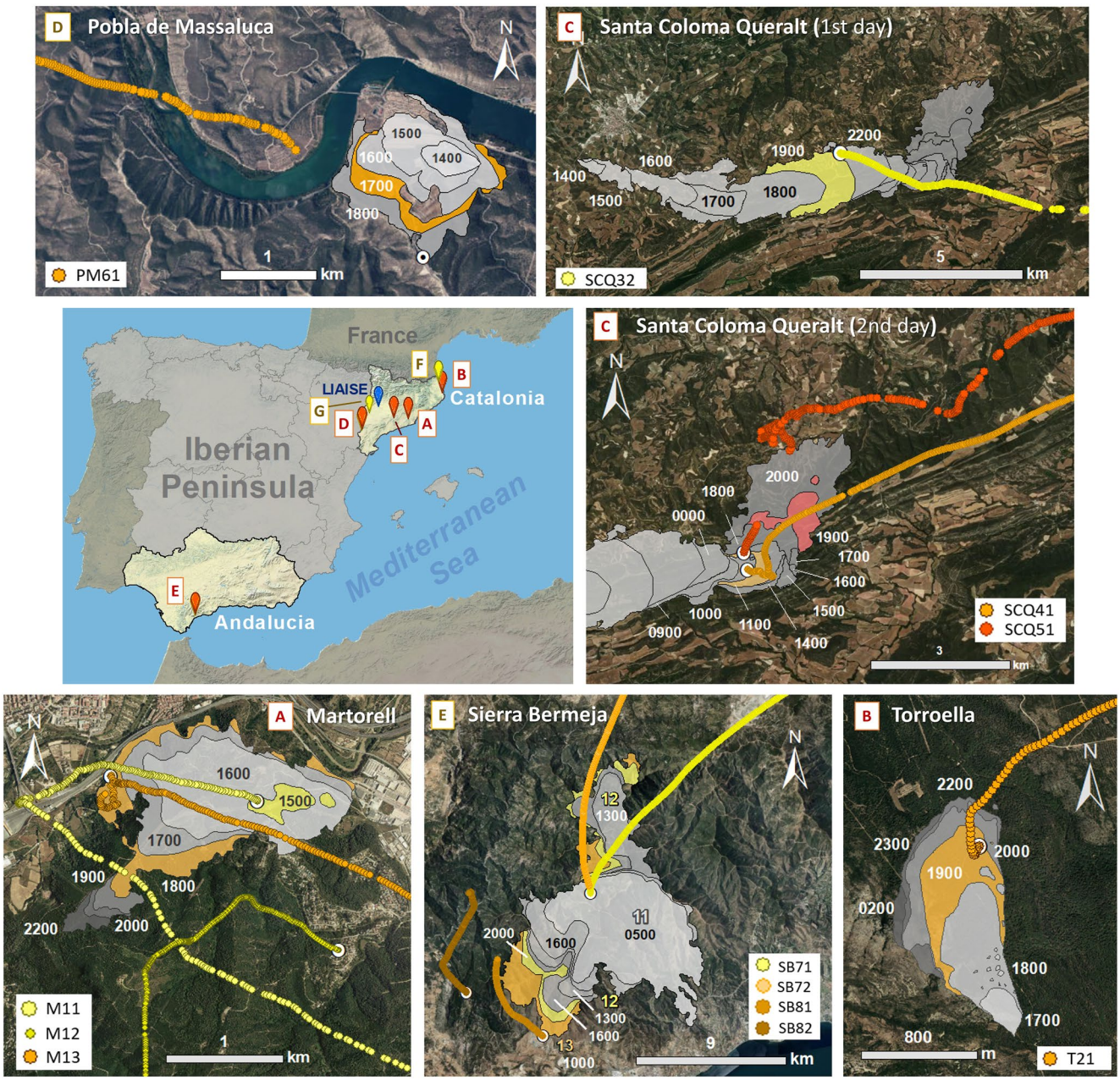

Figure 4. Iberian Peninsula map with the seven fire locations. On orange, the fires where sonde data is completed. On yellow fires where the sonde data is partially completed. We mark the MeteoFrance/LIAISE official radiosounding 2021 site in blue. Every fire perimeter, isochrones, and sondes launching sites and trajectories are included to clarify the position and moment of the fire-atmosphere interaction captured by the sonde. Please note that figures are not at the same scale to facilitate reading.

3.1. Observed Fire Behavior Characteristics

The fire spread biases, identified by comparing between observed and modeled FLI, are presented in Figure 5 as the fire behavior metric to assess the impact of fire-atmosphere interaction.

Both distributions, modeled and observed FLI, peak around $4 \cdot 10^3$ kW·m^{-1}, showing a mid-level FLI to dominate through the 2021 fire season. However, the observed distribution is skewed to the right (1.31–2.37), following the pyroCu distribution. It is important to highlight that those pyroCu events, although they show the distribution with the skewed difference between observed and modeled FLI, were not the highest events registered.

To understand the extreme events, in Figure 6, we compare modeled and observed FLI profiles for each fire to identify FLI biases that can be classified as extreme moments. In addition, we annotate times of observed pyroclouds (pyroCu or pyroCb) which sonde measurements have characterized. Biases in FLI (Figures 6a–6d) are linked to pyroconvection moments, including no pyroCu convective plumes. The only exception is for the Pobla de Massaluca fire (Figure 6e). In this case, the low FLI values can be explained due to the agricultural field pattern, which limited fire spread and reduced fire fronts to flanking and backing behavior.

PyroCu events coincided with FLI exceeding $1 \cdot 10^4$ kW·m^{-1}, the point at which firefighting capacity is overwhelmed (Tedim et al., 2018). Nevertheless, non pyroCu convective plumes observed at Torroella (Figure 6a) and Santa Coloma de Queralt (Figure 6b) also showed high FLI biases, including the maximum FLI recorded during our campaign, with $5 \cdot 10^4$ kW·m^{-1}. Our observations reinforce the idea of linking overwhelming fires to the occurrence of all pyroconvective event types.

The range of FLI observed varied between fires making direct comparisons between them difficult. We normalized the values to solve this variability (Figure 6f), dividing observed by modeled value. The results show that the ratio averages 1, suggesting that extreme fire behavior (values >> 1) occurs during short pyroconvective events amid normal spreading fires (values = 1).

As an example, in Figure 6d, although pyroCb generated a relatively low $1.8 \cdot 10^4$ kW·m^{-1} of FLI, it yielded changes in fire ROS by a factor of 34. In contrast, Figure 6b shows a pyroconvective plume producing $5 \cdot 10^4$ kW·m^{-1} but a normalized ratio of 4.2. The fire in Figure 6b was an already intense fire that pyroconvection accelerated, but the fire in Figure 6d was a low-intensity fire transformed into an extreme fire suddenly by pyroCb formation.

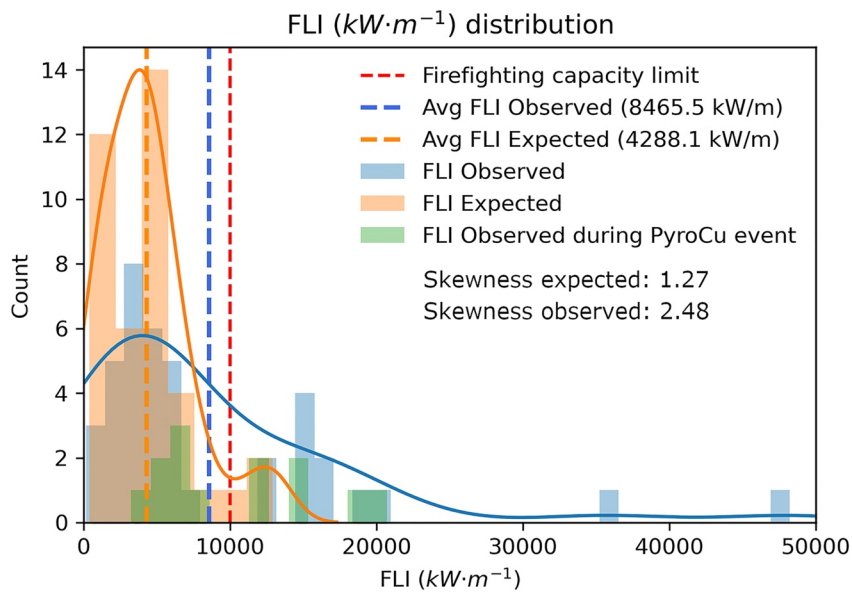

Figure 5. Observed and modeled hourly fireline intensity (FLI, kW·m^{-1}) distributions compared with observed pyroCu events distribution. The modeled FLI distribution has a mean of 4,288 kW·m^{-1} (orange line) compared with the 8,465 kW·m^{-1} of the observed FLI distribution (blue line). The green data set is the portion of the observed data set when a pyroCu was observed. The plot shows how the observed distribution is skewed to the right following pyroCu events distribution.

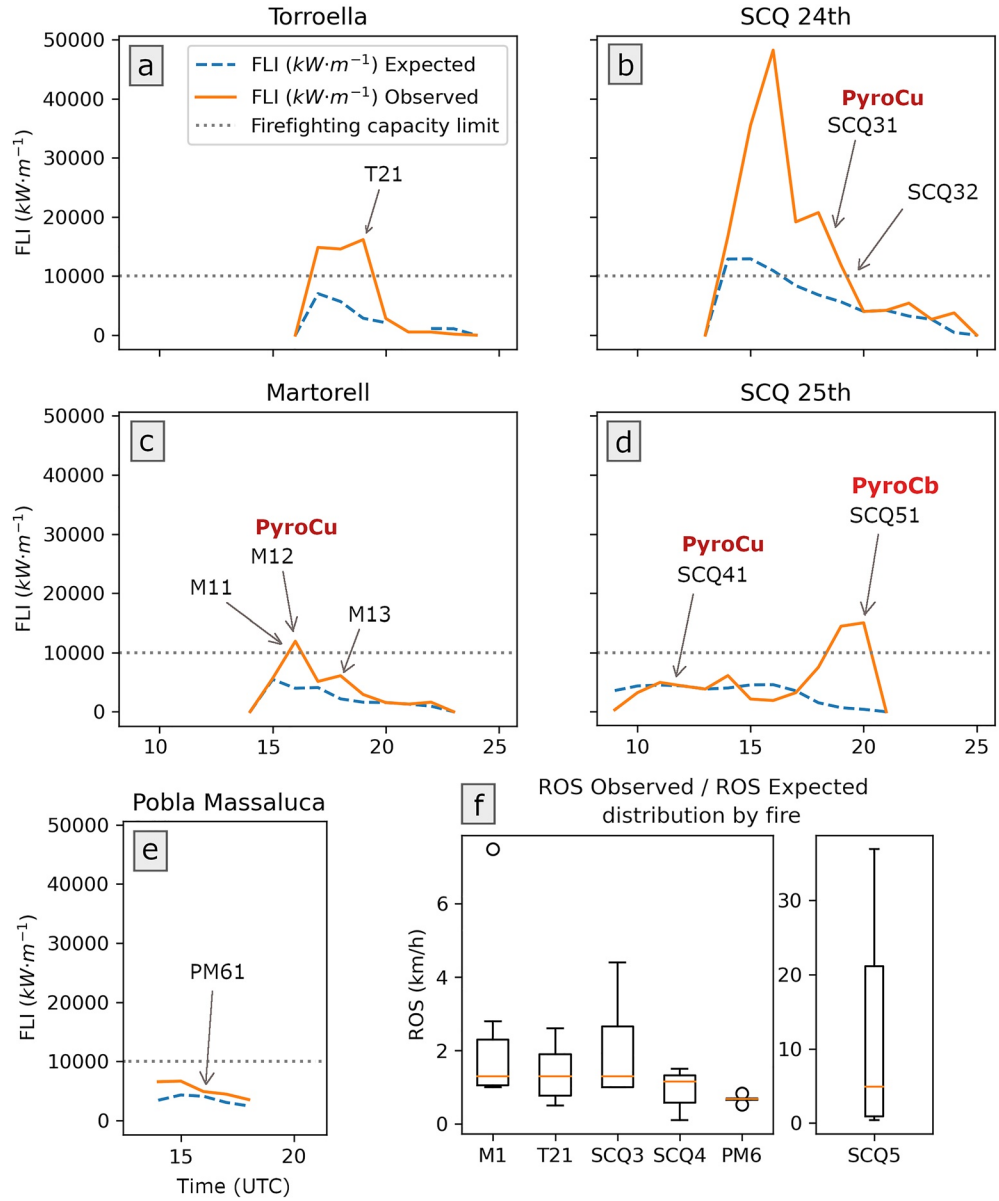

Figure 6. Observed fireline intensities (FLI) in $kW{\cdot}m^{-1}$ in every fire compared with the modeled fire behavior using surface conditions. Every fire is labeled by pyroconvection type observed and sonde launching moment. We show FLI limit for firefighting capacity at $1 \cdot 104$ $kW{\cdot}m^{-1}$ (Tedim et al., 2018). (f) A final boxplot shows the observed versus modeled FLI ratio for each fire. The "o" markers are outliers of the data set. Note that SCQ5 has had to be represented by a subplot due to its scale difference.

Our results suggest that using normalized values is critical to our extreme event analysis. It is important to clarify that the fire-atmosphere interaction needs to be analyzed by the ratio of change in fire behavior variables to allow intercomparison between fires.

3.2. Initial Monitoring Plume and ABL Characteristics

The pyroconvective events identified in Figure 6 by FLI biases are analyzed in Table 1, looking for conditioning variables to draft out our pyroconvective prototypes. We combine for every event the visually observed plume stages and characteristics as in Figure 1 with ERA5 modeled mixing layer values.

Journal of Geophysical Research: Atmospheres
10.1029/2022JD036920

Table 1
First-Order Description for Successful Sondes Launched During 2021 Fire Season

Fire	Pyroconvective event	Type of pyroconvection	Hour (UTC)	Plume stages			Plume characteristics				ERA5 profile stability		LCL/ABL		Shear/ABL	
				Surface	Penetration	Deepening	Overshooting	Flattened plume	PyroCu	PyroCb	$\partial\theta/\partial z$ ($K \cdot m^{-1}$)	γ ($K \cdot m^{-1}$)	ERA5	Observed	ERA5	Observed
Martorell 13 July 2021	M11	PyroCu	16:05		Deepening		Y	Y	Y	N	$2.6 \cdot 10^{-5}$	$4.2 \cdot 10^{-3}$	0.83	<1	0.99	>1
	M12	PyroCu	16:18		Penetration		N	Y	Y	N	$2.6 \cdot 10^{-5}$	$4.2 \cdot 10^{-3}$	0.83	<1	0.99	>1
	M13	Plume	17:02		Penetration		N	N	N	N	$3.7 \cdot 10^{-3}$	$1 \cdot 10^{-5}$		>1		>1
Torroella 22 July 2021	T21	Plume	18:41		Penetration		Y	Y	N	N	$5.4 \cdot 10^{-3}$	$5.1 \cdot 10^{-3}$	4.27	>>>1	2.65	>1
Santa Coloma de Queralt 24–25 July 2021	SCQ31	Plume	19:14		Penetration		Y	Y								
	SCQ32	Plume	19:41		Penetration and momentaneous deepening		N	N	Y	N	$2 \cdot 10^{-3}$	$1.6 \cdot 10^{-3}$	1.35	>>1	0.84	<1
	SCQ41	PyroCu	10:33		Penetration and momentaneous deepening		Y	Y	Y	N	$3 \cdot 10^{-4}$	$5.1 \cdot 10^{-3}$	1.06	>1	0.90	=1
	SCQ51	PyroCb	18:19		Full deepening into free convection		Y	Y	Y	Y	$0.7 \cdot 10^{-3}$	$3.9 \cdot 10^{-3}$	0.97	=1	0.95	=1
Pobla Massaluca 12 August 2021	PM61	Plume	15:02		Penetration		Y	Y	N	N	$4.2 \cdot 10^{-3}$	$7.2 \cdot 10^{-3}$		>>1		<1
Sierra Bermeja 8–12 September 2021	SB71	PyroCu	21:15		Penetration		Y	Y	N	N	$6.3 \cdot 10^{-3}$	$2.6 \cdot 10^{-3}$		>1		<1
	SB81	Plume	05:11		Penetration		N	N	N	N	$9.5 \cdot 10^{-3}$	$2.8 \cdot 10^{-3}$		>1		<1
	SB82	Plume	08:06		Penetration		Y	Y	Y	N	$3.4 \cdot 10^{-3}$	$3.4 \cdot 10^{-3}$		>1		<1
	SB83	Plume	09:13		Penetration		Y	Y	N	N	$5.6 \cdot 10^{-3}$	$3.4 \cdot 10^{-3}$		>1		<1

Note. We show the data of the fire stages, atmospheric boundary layer (ABL) characteristics, and mixed layer thermodynamics as in Figure 1. Pyroconvective events are labeled following the logic of fire acronym, order of event for the season, order of subevent. An orange shadow identifies the environment sondes, outside the fire indraft. ERA5 data is the modeled vertical profile for the sonde hour and launching location, used by prediction capacity during the campaign. The observed ABL, lifting condensation level (LCL), and shear levels are expressed by ratio since their height is estimated on the observation capacity at this first description stage.

The first ABL condition that differentiates pyroconvective types is the stability of the mixed layer, based on θ-gradient from ERA5. For example, the stable ABL situations during pyroconvective event T21 with θ-gradient $>1 \cdot 10^{-3}$ K·m^{-1} represent a non pyroCu convective plume only reaching the penetrating stage. In contrast, pyroCu events M11, SCQ41 and SCQ51 show deepening stages and are well-correlated with neutral or unstable θ-gradient $\leq 1 \cdot 10^{-3}$ K·m^{-1}.

The second condition that differentiates pyroconvection types is LCL height. When LCL/ABL height ratio is >1, fire plumes from intense wildfires can create a deep convective plume with short-living pyroCu. Here we have coined the term "overshooting pyroCu" to name the brief pyroCu pulses that happened in pyroconvective event SCQ32. Meanwhile, pyroconvective events with LCL/ABL<1 will create a "resilient pyroCu", lasting tens of minutes, as observed during pyroconvective event M11.

Further evolution of the pyroCu depends on a third conditioning variable: $\gamma\theta$. This is the main characteristic that supports pyroconvective event SCQ51, with a low $\gamma\theta$ of $3.9 \cdot 10^{-3}$ K·m^{-1}, which evolves to deep moist pyroconvection reaching a "deep pyroCu" or almost a pyroCb. While in contrast, pyroconvective event SCQ41 with a higher $\gamma\theta$ ($5.1 \cdot 10^{-3}$ K·m^{-1}) shows an inhibited pyroCu growth.

The fourth observed condition is maximum wind shear height. When wind shear appears at a distant height from LCL, it inhibits the vertical plume development process, tilting the plume into a flattened angle. For example, in pyroconvective event M11, shear above the LCL and ABL yields to shearing of the already developed pyroCu, preventing further development. On the other hand, when shear height is close to LCL, deepening into the free troposphere is increased by the enhancement of turbulence driven by the local shear. This fact is observed in pyroconvective event SCQ51, where despite strong shear, its coincidence on top of ABL with LCL allows deep pyroCu/Cb to occur.

Overshooting appears to be the fifth condition in pyroconvection. In short, it accelerates penetration or transition to deepening, possibly by strengthening the mixing or entrainment processes. This overshooting is linked to sudden heat flux emitted due to fire activity increase after changes in fuel, meteorology, or terrain. Its key role was observed in all cases, and especially in pyroconvective event SCQ32, where the deep convective plume developed up to 2,400 m despite having a stable θ-gradient $= 3 \cdot 10^{-3}$ K·m^{-1}.

3.3. First Pyroconvection Prototypes

After conducting the conditioning variables analysis, the results from 144 hr of plume monitoring were synthesized and presented in Figure 7, producing the first pyroconvection prototypes. The figure organizes pyroconvective events in order of increasing pyroconvection activity and mixed layer instability. In addition, another clear trend appears, consisting of increasing turbulence (shear and LCL) height closeness to ABL top.

The identified prototypes include "surface plume" (Figure 7a), as the initial or final stage of pyroconvection during which fire interaction is limited to the surface layer. Pyroconvection types start without cloud formation, namely "convection plumes" (Figure 7b). Those plumes present a clear height ratio of LCL/ABL >1.

PyroCu types start with "overshooting pyroCu" (Figure 7c), a short-lived pyroCu that forms in a slightly stable ABL. This pyroCu, having a height ratio LCL/ABL > 1 can only occur following a plume overshooting. Persistent pyroCu appear in unstable ABL and are characterized by "resilient pyroCu" (Figure 7d), which forms in ABL with a height ratio LCL/ABL < 1. This type uses favorable conditions that facilitate permanent condensation but is limited in its vertical growth by shear or stability ($\gamma\theta$) within its upper layers. Finally, a "deep pyroCu" or a "pyroCb" (Figure 7e) happens when a pyroCu development breaches the atmospheric cap and attains a free convective state.

In our diagram in Figure 7, another possibility can be drawn if we consider a repeated overshooting pyroCu. In this dry convection case, persistently overshooting creating moist pulses could transform situation Figure 7c into Figure 7e, the pyroCb type. It is an extreme case, depending on a sustained overshooting due to an increased fire behavior by a continuous change in fuel or topography. Although not observed in our 2021 campaign, similar cases have been described in the literature (Tory et al., 2018).

The importance of every pyroconvective event can be assessed by considering the relative number of hours each pyroCu prototype was observed. Details are presented in Figure 7, accounting for pyroCu activity duration in fires

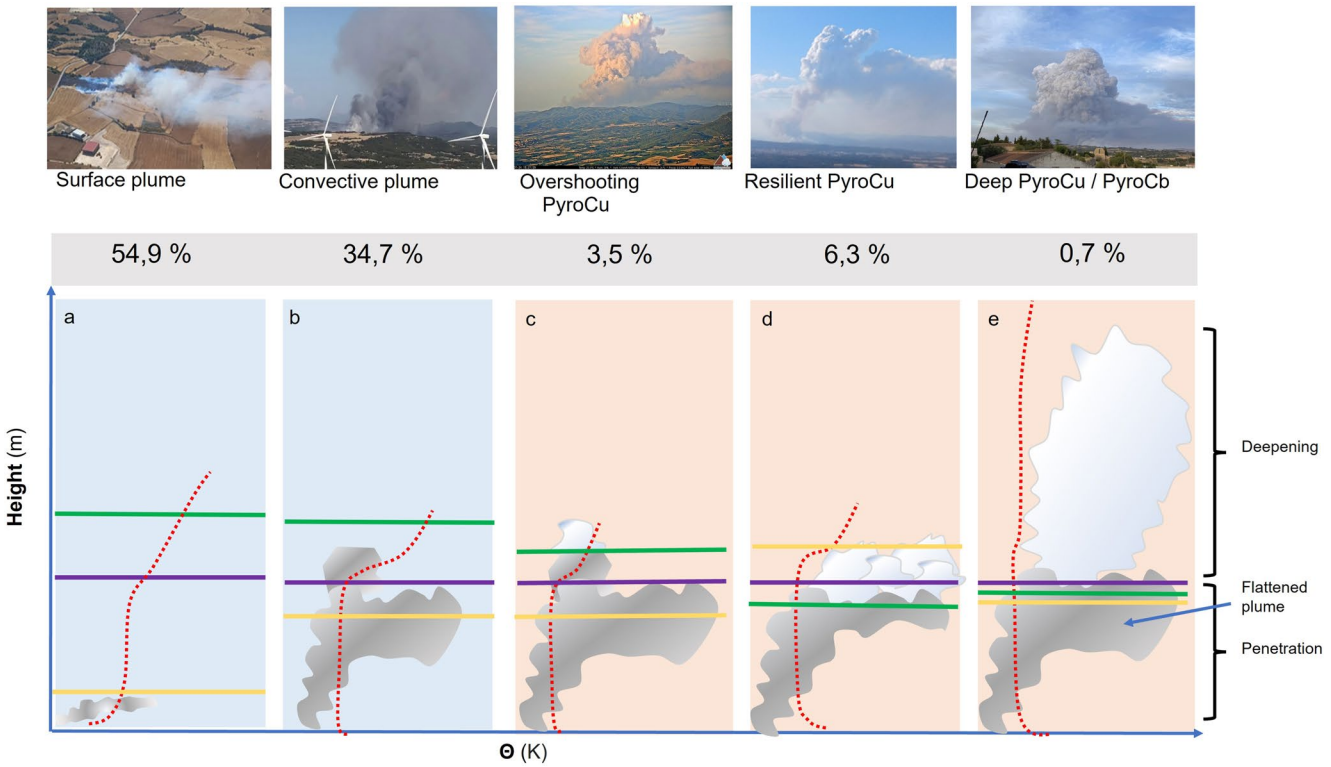

Figure 7. Pyroconvection prototypes observed during our 2021 campaign were illustrated by a picture of a real plume and a scheme of the conditioning variables from Table 1. The frequency expresses the proportion (%) of fire hours of every pyroconvective type observed during the 144 hr monitored in our campaign. The red line represents the θ profile, violet level the atmospheric boundary layer top, green level the lifting condensation level, orange level the wind shear. The back color shows the intensity of fire behavior change observed when the pyroconvection prototype is present.

that had shown pyroconvection activity. Surface fire type, with no pyroconvection, represents 54.9% of observed fire hours. If we consider the convective plumes, fire spread hours without pyroCu account for 89.6%. PyroCu types are only present in 10.5% of fire hours, and deep convection is restricted to 0.7%. Our findings support the idea of pyroCu formation as singular and rare events (Potter & Hernandez, 2017). The final percentages for every prototype considering all fire season activity will be much lower since our data set only contains data of successfully pyroconvective fires during 2021 fire season, representing 0.012% of 2021 fires (GENCAT, 2021).

3.4. Fire-Atmosphere Interaction Induced Changes in Vertical Thermodynamics

After classifying the observed pyroconvective events into different prototypes, we analyze each prototype's changes induced by fire-atmosphere interaction.

First, we compare in-fire sondes with environment sondes. Second, we evaluate plume deepening above ABL as a process that can reinforce entrainment. Third, we analyze changes induced on ABL thermodynamics that create the new fireABL as a final step of the fire-atmosphere interaction.

3.4.1. Comparison of the In-Fire Plume and Outside Plume Sondes

We compare sondes M11, M12, and M13 from the Martorell fire on July 13 (Figure 8). Sonde M11 (in-fire plume) reached the fireABL top in 8 min, showing condensation as a pyroCu. M12 (outside but underneath the fire plume) took 15 min to attain M11 altitude, finally reaching the plume's flattened top layer. M13 (sounding near the fire during a non-pyroconvective event) was sheared at a lower altitude, not reaching ABL top. M11 is the only one that measured a descent for 10 min of the flight. During the 10 descending minutes, the sonde was embedded within the pyroCu, indicating a downdraft of the pyroCu dragged it.

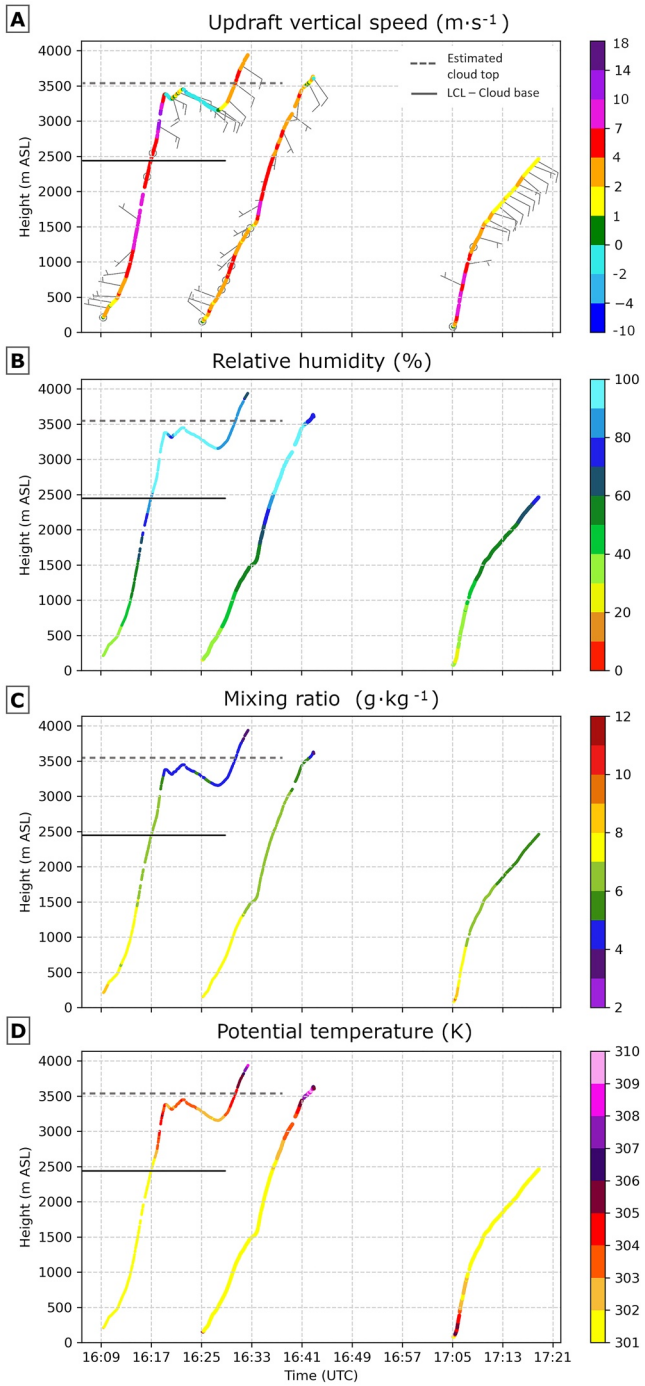

Figure 8. Sonde M11, M12, and M13 ascending paths comparing the in-plume-modified atmosphere (M11) and outside plume M12 and M13. M12 launched outside the fire but underneath the influence of the pyrocloud. M13 was launched outside the plume and outside the influence of the pyrocloud. We show profiles of (a) updraft vertical speed ($m \cdot s^{-1}$), (b) relative humidity (%), (c) mixing ratio ($g \cdot kg^{-1}$), and (d) θ (K).

Comparing the state variables, we found that the θ values, averaged over the ABL depth, were very similar for all profiles, whereas moisture observations showed differences. M13 had a high q of 9 $g \cdot kg^{-1}$ at the surface but a relatively low q higher up in the atmosphere. In this profile, the surface was influenced by the sea breeze from the east, whereas the air higher in the ABL was dry continental air from the west, explaining this difference in q. This q profile skewness is less visible in the profile of M12 and especially M11, which shows a well-mixed profile and a higher average q.

Figure 8 provides additional information concerning increased entrainment induced by pyroCu into the sub-cloud layer. M11 shows that θ inside the downdraft is cooler than at the same height during updraft or nearby M12 sonde. Next to this, the q in this downdraft part of the profile is slightly higher than the q at the same height in the updraft, just before the radiosonde reached the downdraft. This fits the theory of evaporative cooling. Near the edge of the pyroCu cloud, the saturated air evaporates, requiring energy and thus cooling down the air while simultaneously moistening it. With the colder air, the air subsides and causes entrainment into the fireABL. This entrainment of more moist air into the fireABL likely explains why the profile of M11 is less skewed than the other profiles and has a higher q.

Although a sea breeze is also a possible cause of an increase in humidity, here, all three profiles were under the influence of the sea breeze. Consequently, the higher q in M11 cannot be explained by the sea breeze, making it likely that the increased humidity is produced by entrainment from the pyroCu layer. Because of the spatial and temporal proximity of all three profiles, it is unlikely that any difference is produced by local effects.

3.4.2. Fire Reinforced Entrainment Characterization

A comparison between fire sondes ascending paths during each of the pyroconvection types is presented in Figure 9. The updraft vertical speed ($m \cdot s^{-1}$) is color-coded to evaluate a theoretical parcel travel time in Figure 9a. Figure 9b shows the RH (%) to differentiate between dry and moist convection. Levels of LCL and ABL predicted by ERA5 and observed fireLCL and fireABL by fire sonde are also shown, characterizing the deepening stage of the plume.

First, our results highlight that observed fire-induced deepening leads to much higher entrainment than average convective boundary layer conditions, which are assumed to deepen above mixing layer height at 20% of the ABL depth (Stull, 1988).

Second, we observe that deeper plumes occur when the fireLCL/fireABL height ratio is close to 1 (Figure 9), further supporting the results of the pyroconvective prototypes shown in Figure 7. Interestingly, plume deepening and updraft vertical speed increased with the deepening of moist convection. This observation suggests that dry convective plumes without pyroCu harness their overshooting strength from fire intensity-induced buoyancy, but moist convection types harness additional buoyancy from processes such as latent heat release during pyroCu formation.

When comparing the rising profiles in Figure 9b, we can observe that those with height ratio LCL/ABL > 1 show low RH below 80% near the top of ABL in contrast with higher RH above 90% when height ratio LCL/ABL < 1. Consequently, the plume-reinforced entrainment of dry or moist air from above fireABL into the fire mixed layer is key to whether a dry or moist convection regime may occur. We can see that sondes T21, SCQ32,

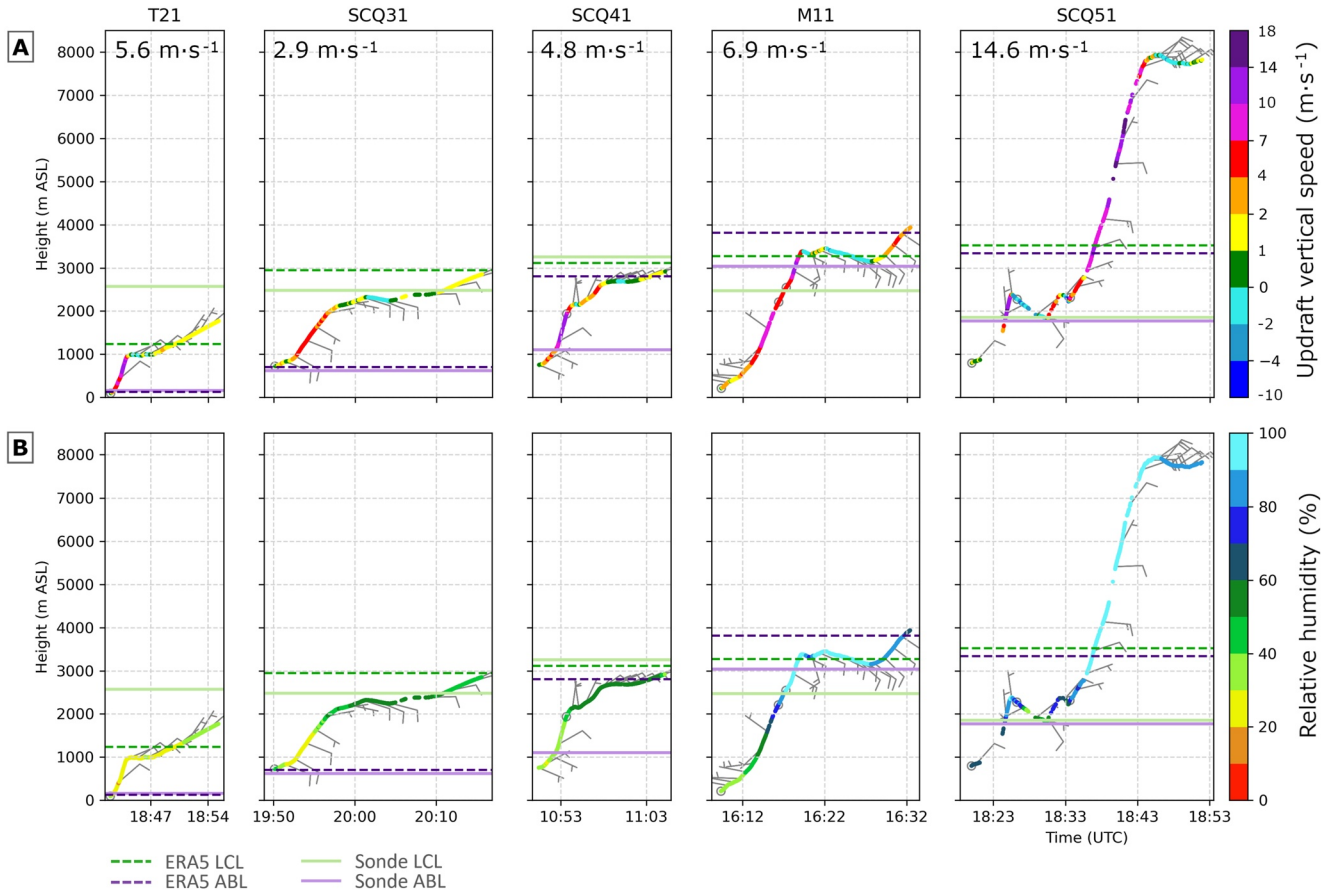

Figure 9. Rising profiles from fire sondes (Table 1) for pyroconvection prototypes (Figure 7). lifting condensation level and atmospheric boundary layer height (dashed is ERA5 and solid is fire-sonde) are also indicated. (a) Radiosonde updraft vertical speeds for pyroconvective measured events. The average travel time is included on top of every case. In addition, the horizontal wind speed and direction (wind flags) are included. Considering an average ascension balloon speed of 1.5 $m \cdot s^{-1}$, a descending bit is signaled by green and blue colors. (b) The same rising profile trajectory but showing relative humidity (RH).

and SCQ41 indicate a dry convection regime with RH < 90% on top of the plume, and moist convection types are represented by M11 and SCQ51 with RH > 90% in their pyrocloud layer.

Additionally, the identified convective regimes driven by entrainment were also associated with regions of descending air near the top of every pyroconvective plume or pyrocloud. This finding, originally observed in Figure 8, is also observed in all in-fire sondes of Figure 9 and is likely adding to an already increased entrainment. Descent regions were defined herein as rising speeds below the average ascent speed of the sonde (1.5 $m \cdot s^{-1}$). We can observe significant differences in duration and intensity between dry (Figures 9a–9c) and moist (Figures 9d and 9e) convection cases. SCQ31 was an ideal case for observing this behavior during a dry convective regime where the sonde descended for 3 min after the plume had flattened. On the contrary, the moist convection case represented by M11 showed a downdraft duration of nearly 10 min.

3.4.3. Fire-Atmosphere Interaction Induced Changes in the FireABL

Now we evaluate the type of changes in the initial ABL thermodynamics that the enhanced entrainment by pyroconvection prototypes creates.

To assess those changes, in Figure 10, we compared the in-fire sondes with ERA5 vertical profiles for each pyroconvection prototype defined in Figure 7. We include θ, q, LCL, and ABL heights from ERA5 for the time of the sonde and ±1 hr to analyze differences between the ABL and the fireABL dynamics. We left the "surface plume" type out of the analysis as it does not modify ABL thermodynamics.

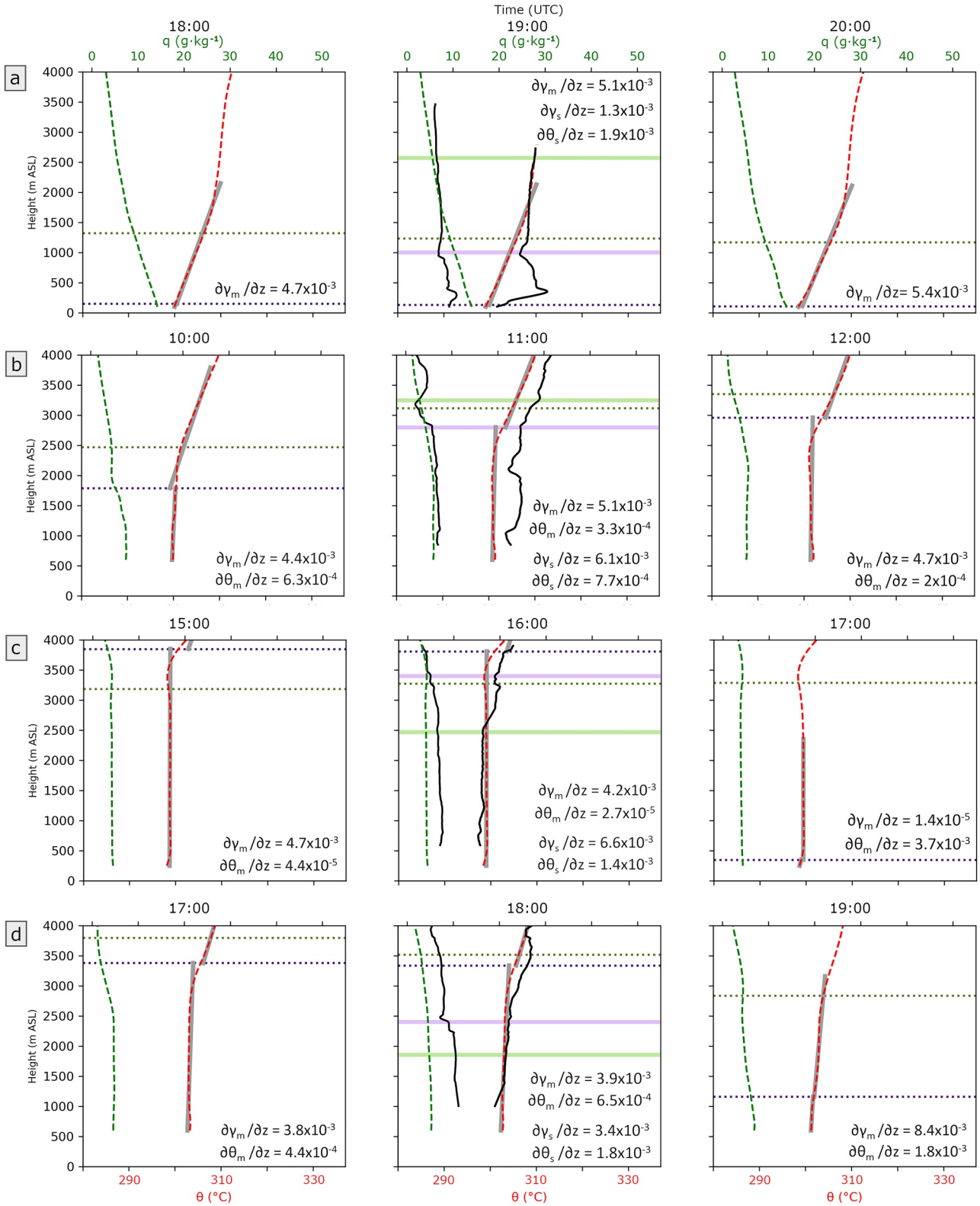

Figure 10. Fire sonde and ERA5 profiles for every prototype as in Figure 7. Comparison of ERA5 θ (red) and q (green) profiles with black lines representing the sonde data. Levels are represented by horizontal lines, being atmospheric boundary layer the violet line, and lifting condensation level the green line. The solid lines represent sonde levels. The dashed lines are the model ERA5 levels. (a) Convective plume (sonde T21), (b) Overshooting pyroCu (sonde SCQ41), (c) Resilient pyroCu (sonde M11), (d) Deep pyroCu/pyroCb (sonde SCQ51). The numbers show the θ gradient for the mixed layer and free atmosphere. Suffix "m" means modeled ERA5 data. Suffix "s" means sonde profile data.

Regarding the "convective plume" type without pyroCu formation, we analyze the T21 fire sonde (Figure 10a) profile launched at the Torroella fire on July 22. With a θ-gradient of $4.7 \cdot 10^{-3}$ K·m^{-1} it had a stable profile with a LCL 1,400 m higher than ABL. However, we can observe how the fire plume deepens up to 900 m (Figure 9a T21), which seems to cause an unstable mixing layer showing a new θ-gradient of $1.9 \cdot 10^{-3}$ K·m^{-1}. Also, this entrainment of dry air around 30% RH resulted in a drier, hotter mixed layer that, in turn, increased fireLCL height (Figure 10a).

The Santa Coloma Queralt sonde SCQ41 launched on 25 July (Figure 10b) captured the "overshooting pyroCu" type. Although the ABL was unstable with a θ-gradient of less than $1 \cdot 10^{-3}$ K·m^{-1}, the LCL was 500 m above ABL. Plume overshooting was entraining dry air and could only rise above fireLCL for a short period. As in the previous case, the fire-induced changes increase fireLCL and θ when compared to the environment.

Martorell fire sonde M11 on 13 July (Figure 10c) represents the "resilient pyroCu" prototype. It had an unstable ABL of $2.7 \cdot 10^{-5}$ K·m^{-1} that fire changed to $1.4 \cdot 10^{-3}$ K·m^{-1}. In this example, the changes are reversed, having an LCL below ABL in an unstable θ-gradient, with a 500 m deep pyroCu formed permanently over the plume. As a result, plume overshooting deepening above ABL formed a moist convection regime that increased specific humidity by 2 g·kg^{-1}. New fireLCL height was decreased by 800 m, enabling deepened pyroCu formation.

The Santa Coloma Queralt sonde SCQ51 on 25 July (Figure 10d) represents the "deep pyroCu/Cb" prototype. It showed the same unstable ABL modification to neutral stability seen in previous sonde M11 fireABL. However, this case observed similar LCL and ABL heights favored enhanced deepening above ABL, which in this case achieved 8,000 m.a.s.l. Fire-induced changes due to deep pyroCu formation produced an enhanced moist convection regime that reduced fireABL (1,000 m) and fireLCL (1,800 m) height and increased q in 6 g·kg^{-1}.

Fire-induced changes in θ and q profiles and fireLCL and fireABL height were observed in all profiles in Figure 10. Specific humidity values were higher than environment values in the moist convection types. Being 2 to 6 g·kg^{-1}, they were well above the value proposed by Luderer et al. (2009), (0.2 g·kg^{-1}) but more in line with Potter (2005), (2 g·kg^{-1}). Luderer's case seems to correspond to our dry convection type. Temperature values of θ show the differences the other way around. Dry convection increases θ by 2–3 K, according to what is proposed by Potter (2005), but moist convection stays close to the values proposed by Luderer et al. (2009). Changes in ABL and LCL height are also observed to differ between moist and dry convection. Our results show an increase of θ and fireLCL height in dry convection regimes, as shown in Figures 10a and 10b, in contrast to an increase of q and a decrease of fireLCL height in moist convection regimes, as in Figures 10c and 10d. The differences in the values proposed in the literature to compute fireCAPE and the real ones measured by in-plume fire sondes highlight the need for in situ measures.

3.5. Fire Spread Changes Correlation With Modified FireABL Thermodynamics After Fire-Atmosphere Interaction

For each described prototype (Figure 7), we explore how modified fireABL after fire-atmosphere interaction affected the fire spread pattern.

In Figure 11, we show the different effects of the fire-atmosphere interaction over the fire spread pattern when we correlate observed hourly ROS (km·h^{-1}) to the hourly burnt area (ha·h^{-1}). Our result indicates that moist pyroconvection expands the burnt area without increasing the ROS proportionally. In contrast, dry convection events show a sharp increase in the ROS, not followed by an increase in the burnt area. Santa Coloma de Queralt PyroCb data provided evidence of a moist convection effect when the surface burn ratio increased from 90 to 295 ha·h^{-1}. However, they maintained ROS between 1.2 and 1.8 km·h^{-1}. The Santa Coloma de Queralt oPyroCu data show a representative case of dry convection effect with an average 100 ha·h^{-1} burnt area ratio that correlates with a ROS increase from 2 to 6 km·h^{-1}. It is important to stress that all fires were evolving in complex terrain, but the pattern shown in Figure 11 is consistent in all fires despite the differences in topography and fuel type. Furthermore, our study's major runs in moist pyroCu occurred downhill (M11 and SCQ51), suggesting that pyroconvection is not caused by slope-induced acceleration (see Text S3 and Figure S2 in Supporting Information S1).

Despite the importance literature gives to fireCAPE as a metric to assess pyroCu effects, it is known to be a difficult variable to estimate (Tory & Kepert, 2020). To compute it, we have made two assumptions. First, we need to complete the fire sonde profile in the upper part until the EL (equilibrium level) using ERA5 profile data. Second, in the absence of in-plume sonde data, we need to estimate the surface fire-induced conditions on θ.

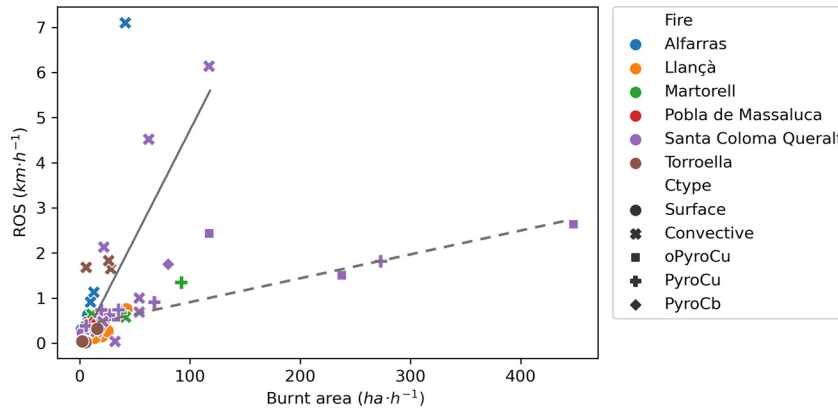

Figure 11. Correlation between surface burnt area ($ha \cdot h^{-1}$) and the observed rate of spread (ROS, $km \cdot h^{-1}$) for every hour of pyroconvective event. Data points on the correlation are colored by fire, shape is assigned for pyroconvective type. The correlation shows two divergent trends: (1) continuous line shows an increase in ROS without significant change on the burnt area (narrow and elongated fire perimeter). It represents the spread type by convective plumes under a dry convection regime. (2), the dotted line follows a trend of increasing burnt area without significant change in ROS. This second type is dominated by moist pyroconvection and the different pyroCu types.

To overcome these limitations, in Figure 12, we correlated normalized ROS (Figure 6f) with fireCAPE and updraft vertical speed variable as in Figure 9a. Estimated fireCAPE shows a satisfactory correlation ($r^2 = 0.68$). However, we find a more accurate correlation ($r^2 = 0.905$) between the updraft vertical speed and ROS ratio. The correlation between updraft vertical speed and ROS ratio unifies moist and dry convection and confirms moist convection as the pyroconvection type creating the most dramatic change in fire spread.

Our result suggests a clear metric to translate pyroconvection effects into fire behavior changes to be expected. Indeed, the updraft vertical speed is a variable that can be directly measured in situ in fire incidents to assess fire spread changes to be expected during pyroconvection events.

4. Discussion

Our fire monitoring campaign identified a direct relationship between fire FLI and ROS biases and different types of pyroconvection. Furthermore, the observations suggest that the fire-atmosphere interaction causes a complex dynamic cycle composed of four main stages, further discussed and integrated into this section:

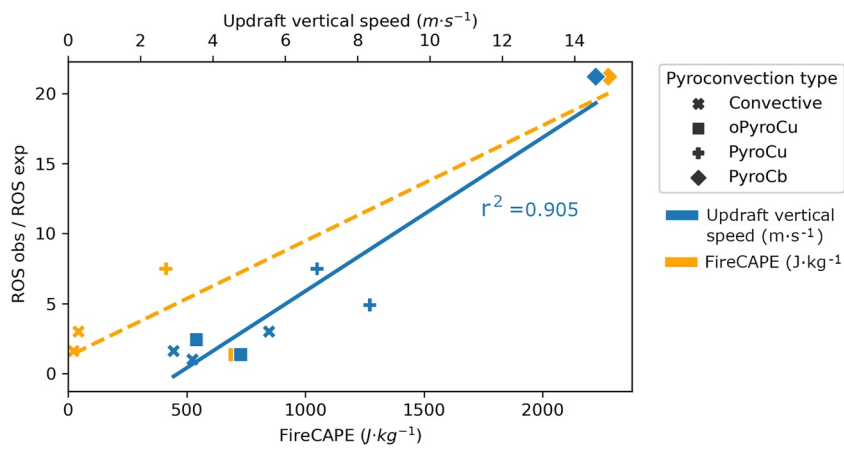

Figure 12. Quantitative correlation between fireCAPE (orange) and updraft vertical speed (blue) with rate of spread (ROS) bias. The data has been classified with the proposed prototypes of pyroconvection. FireCAPE has been obtained by computing the CAPE over the profile measured by the sonde and complemented using ERA5 profile data with the surface value measured by the sondes.

1. The ABL thermodynamics interact with fire intensity, conditioning plume overshooting.
2. Plume overshooting and pyrocloud formation increase entrainment from the pyroCu layer into the sub-pyroCu layer, inducing moist or dry convection regimes in the ABL.
3. Induced convection regime changes original ABL thermodynamic conditions.
4. New fireABL thermodynamic conditions induce changes in fire behavior.

4.1. Preconditions of ABL Thermodynamics to Favor pyroCu Formations

We have investigated the plume-driven fire type in detail, identifying four prototypes; three of them are variations of the pyroCu types. The classification was obtained by combining visual plume observations, θ-gradient in the mixing layer, and the relative plume height with respect to ABL and the LCL height. The θ-gradient in the ABL, as a measure of thermodynamic stability, and wind shear are the variables that separate wind-driven from pyroCu-driven fires (Finney et al., 2021) and condition the capacity of the plume to penetrate ABL through buoyancy consumption (Potter, 2002). We have observed that this penetration height was controlled by the ABL stability (θ-gradient), but also the respective locations of the LCL, ABL and shear height proximity (Figure 9). Under no-fire ABL conditions, this finding agrees with the Pino et al. (2003) study regarding ABL-induced growth by shear location close to ABL height. Recently, Artés et al. (2022) supported the concept of turbulence importance near ABL top. They identified that ABL and LCL closeness in the vertical profile, before the fire, is a variable that is as critical as the surface Fire Weather Index (FWI) values (Van Wagner & Forest, 1987), to explain extreme fire behavior events.

4.2. Increased Entrainment of Free-Tropospheric Air Into the ABL

The resulting plume drives the enhanced entrainment above the ABL. The upper-air measurements (Figure 8) provide evidence that during pyroconvection events overshooting pulses are causing the penetration and deepening stages. The depth of the plume deepening above ABL will determine the intensity and dryness of entrainment. Our observations show higher deepening into the cloud layer with pyroCu formation compared with convective plumes (Figure 9), most likely driven by the effect of latent heat release when pyroCu is formed. This hypothesis is supported by the study by Kuang and Bretherton (2006), who suggest that in cumulus, elevated updrafts are fed by higher entrainment above the cloud base, driven by turbulence around pyroCu condensation.

When comparing the observed fire-atmosphere interaction (Figure 10) with previous studies on clear ABL conditions, the entrainment-induced changes of dry air inside ABL resemble those proposed by van Heerwaarden et al. (2009) to describe land-atmosphere interaction feedbacks. In this context, our convective plumes and overshooting pyroCu type can be connected to entrainment heating and drying feedback. The overshooting above ABL reinforces dry air entrainment, leading to the fireABL height increase. As a result, it creates well-mixed, warmer, and drier vertical profiles. The drier and hotter fireABL was observed in our fire sondes (Figure 10), in agreement with the detailed plume analysis in burn experiments by Arreola Amaya and Clements (2020). In addition, this drying of fireABL increases fireLCL, agreeing with visual, sounding, and radar-Doppler observations by Lareau and Clements (2016, 2017).

A novel result highlighting the effect of plume overshooting-induced changes in entrainment is the cooling regions with a downward motion observed above every pyroconvective plume (Figure 9). These cooling regions were significantly more profound and broader on moist convection plumes, coinciding with the evaporative shell described in shallow cumulus observations (Heus & Jonker, 2008; Rodts et al., 2003). In our analysis, cooling regions appeared as a new distinctive variable explaining enhanced entrainment and creating moistening feedback for fireABL, complementing those feedbacks from van Heerwaarden et al. (2009). In addition, the increased q after cooling cell, lowered the fireLCL while creating deeper pyroCu.

4.3. New Pyroconvective ABL Conditions

The sondes readings (Figure 10) suggest that changes inside fireABL, modifying the thermodynamic state of the well-mixed layer, are driven by enforced entrainment of dry or moist air from the pyrocloud layer.

Supporting the entrainment importance is that fireABL, instead of showing increased instability from fire heating at the surface, shows a mixed layer modification to an almost stable value around 1.10^{-3} K·m^{-1} in all cases.

This is evidenced in SCQ51, where unstable conditions dynamically lead to a reduction of θ-gradient instability, whereas stable conditions, as in T21, yield an increase.

Patterns shown in Figure 10 provide evidence of an increase in θ or q on fire mixing layer profiles depending on induced dry or moist convection. The LCL versus ABL height relative position define the resulting convection regime (Figures 9 and 10). Our observations indicate that when plume-entrainment stays below the LCL, dry convection dominates, causing an increase in θ and creating convective plumes or overshooting pyroCu. However, if plume entrainment penetrates above the LCL, resilient or deep pyroCu will form moist entrainment, increasing q.

It is important to note that dry and moist convection yield changes in fireLCL and fireABL heights. The magnitude of these changes, in particular for the variation of fireLCL, depends on the relative position between LCL and ABL height, quantified by the LCL/ABL height ratio. Our results extend with new observational evidence to the controversy of whether humidity for moist convection is favored by humidity released by burning vegetation (Potter, 2005) or by the amount of humidity in the environment (Lareau & Clements, 2016; Luderer et al., 2006, 2009). Our observational analysis supports the key role of the humidity present in the environment in determining the fireLCL height position. According to our analysis, dry convection-type situations, where LCL/ABL height ratio >1, will increase fireLCL height. However, under moist convection types characterized by LCL/ABL height ratio $\leq$ 1, fireLCL will decrease. Recently, Eghdami et al. (2021) confirmed the importance of environmental humidity as the source of increased plume humidity. The study was conducted based on sensitivity analysis with WRF-FIRE experiments (Coen et al., 2013) reproducing the Santa Coloma de Queralt fire, using our SCQ51 radiosonde data to adjust the model.

4.4. Pyroconvective FireABL Correlation With Fire Spread

The final stage of the fire-atmosphere interaction cycle controls how the changes in fireABL affect fire behavior and change fire spread patterns. Published works relate pyroCu/Cb with changes in fire intensity due to increased slope or fuel load (McRae et al., 2015). The analysis of slope change in the spreading axis of our fires (see Figure S3 in Supporting Information S1) shows that topography change has no correlation with the sudden increase in fire behavior, pointing at the pyroconvection importance in fire spread bias.

The fire spread biases coincided with extreme fire intensities, showing pyroconvection phenomena. These biases are quantified as a ratio between observed and modeled fire behavior, averaging a value of 3 (Rothermel, 1991). Our results (Figure 6f) agree with that proposed ratio value, showing an average of 3.3. However, when we observe deep pyroCu/Cb (0.7% observed fire hours), values range from 4 to 34. Although deep pyroCu/Cb is less frequent, it results in more intense pyroconvective events and more extreme fire behavior, coinciding with previous studies (Fromm et al., 2012; Potter & Hernandez, 2017).

Changes in fireABL also influenced fire perimeter shape. Figure 11 shows that dry and moist convection affected fire perimeter shape differently. This can be explained by the observed cooling region size, duration, and position above the plume. If entrainment happens under the influence of small cooling cells in dry convection regimes, the resulting surface θ-gradient created on the surface layer will increase wind speed in that head fire area, resembling a low-level jet (LLJ). Such an effect can cause an elongated fire perimeter, as reproduced by Clark et al. (1996) in their pioneering fire-atmosphere coupled model. In contrast, the larger size and longer duration cooling region increase q on a broader area in moist convection regimes. The consequent shrinking of LCL height deepens convection and increases the indraft on the surface layer. This process increases fireline intensity in all parts of the fire and creates a more rounded perimeter, an effect consistent with the analysis of fire behavior changes by plume-induced entrainment, as discussed in McAllister (2021).

An important finding of our research has been the confirmation of a correlation between fire behavior change and plume updraft dynamics proposed by Potter (2012). The quantitative correlation between plume updraft vertical velocity with ROS ratio (Figure 12) provides a first quantitative relationship between pyroconvection and fire behavior change. In contrast to the difficulties of accurately estimating fireCAPE (Luderer et al., 2006; Potter, 2005; Tory & Kepert, 2020) the data needed to calculate updraft vertical speed can be easily obtained using inside-plume soundings, profilers, or Doppler readings (Clements et al., 2018). Our results confirm that moist convection events are likely to have a more significant impact on fire spread. Moist convection creates higher

updraft vertical velocity when using added latent heat release after forming a pyroCu. In contrast, dry convection plume updraft depends exclusively on fire-induced overshooting. Such updraft reinforcement coincides with the sudden increase in extreme fire behavior, observed at SCQ51 sonde, when observed versus modeled ROS changed from 3 to 34. Published reports about the 2017 Portuguese firestorms (Guerreiro et al., 2017, 2018) described a similar effect when the plume went from pyroCu to pyroCb after a nearby thunderstorm system forced LCL and shear height close to ABL height.

4.5. Outlook

Our research adds new understanding to the current explanation of how pyroCu affects fire spread. Traditionally, the focus has been set on instability and shear as atmospheric conditions and indrafts and downdraft processes as the final effect of pyroconvection on fire spread (Finney et al., 2021). The observational analysis complements the assumption by Clark et al. (1996) and Charney and Potter (2017) that direct surface heating and drying by the fire front are the main drivers enhancing the buoyancy of fire plume. Our findings reinforce the importance of turbulence closeness at ABL height and propose the increased entrainment induced by plume overshooting as an essential process to create different convection regimes and separate pyroconvection prototypes and their effects on fire behavior.

This study offers an improvement to the available tools and a clear understanding of the physics involved in the pyroconvection types that influence changes in fire spread. In addition, the data collected here can form the basis for large-eddy simulations (LESs) to confirm the validity of our observational analysis and validate our proposed classification.

5. Conclusions

We investigated fire-spread biases under fire-atmosphere interaction and the resulting pyroconvective events. To this end, in the summer of 2021, we deployed a suite of in-plume radiosoundings during seven extreme wildfires and simultaneously in the surrounding environment. These thermodynamic observations complemented the ERA5 model vertical profile. We related these upper atmospheric measurements to direct observations and model calculations of fire spread characteristics to obtain a comprehensive data set and relationships of the fire-atmosphere interaction.

By analyzing the vertical profiles of temperature, humidity, wind, and ABL and LCL heights within the fire plume and comparing this to the environment, we established a new classification of pyroconvection, including convective plumes and overshooting pyroCu as dry convection types and resilient pyroCu, and deep pyroCu/Cb as moist convection types. The main characteristic of the dry convection regime was the increase of the potential temperature (θ) profile within the mixing layer. Under this regime, we observed an enhancement of 2 K compared to the same wildfire environment observed Santa Coloma de Queralt on July 24. Alternatively, observations made at the Martorell fire on July 13, which belongs to the moist regime, increased specific humidity by 3 $g \cdot kg^{-1}$ compared to the environment.

We have found that plume overshooting enhanced entrainment (in form of downdraft) from the pyrocloud layer into the sub-cloud layer will induce dry or moist convection. This entrainment process, caused by plume penetration or deepening, depends on fire intensity, ABL stability, free troposphere lapse rate, and closeness of LCL and shear to ABL height. Two examples enable us the distinct behavior between dry and moist regime. The Torroella fire on July 22 provided an example of dry convection. There, the plume is able to penetrate the stable dry ABL by 900 m but could not reach LCL. As such, the resulting entrainment of dry and warm air warms up the mixing layer. The Martorell fire provided an example of moist convection on 13 July, where plume fully penetrated an unstable mixing layer. This leads to create a pyroCu deepening 400 m above LCL and induce a moist convection regime. Our research also identifies a new entrainment enhancement process in the form of a cooling region on top of every plume that changes entrainment intensity and duration (Figure 9). We also identified that the dry convection regime creates small cooling regions. Characterized by descending motions of the sounding that lasts 2–5 min (tens of meters), while the moist convection regime descending sonde motions lasted 10–30 min (hundreds of meters).

In the seven cases under analysis, and despite the differences concerning the topography and fuel types, we have found similar patterns in the dynamics of the sub-pyrocloud layer. The moist convection types created greater changes in the ROS, also speeding up the fires downhill. In contrast, the more intense runs uphill only created a convective plume or overshooting pyroCu. Therefore, without clearer evidence, we can conclude that terrain-induced accelerations are not a dominant process in forcing pyroCu/Cb formation. On the contrary, our observations suggest that the fire spread changes resulted from the fire-atmosphere interaction induced changes on the ABL. In short, the resulting sub-pyrocloud layer from dry and moist convection regimes consistently created fire spread changes independently of fuel and topography.

We have found an increase that ranges from 2 to 6 in the fire spread ratio between observed and modeled in dry convection types and between 3 and 34 in moist convection types, respectively. The enhancement of the surface fire spread showed a quantitative correlation with the plume updraft vertical speed ($r^2 = 0.905$) when including all observed cases of moist and dry convection regimes. However, differences appeared in the patterns of fire growth. Dry convection created a narrow and elongated spread pattern, while moist convection created a fire spread pattern that yielded head and flank fire fronts.

This analysis shows the strong value of using in-fire-plume soundings to advance understanding of the coupling between upper air atmosphere and fire spread. In-fire sondes can complement measures done with radar-Doppler. The comprehensive observational set, the pyroconvection classification, and this first quantitative correlation are important steps to improve models that coupled surface fire to atmospheric thermodynamics, analysis reliability, and safety during extreme fires. This methodology and valuable collaboration between science and fire management practice facilitate firefighters' shared observation of the phenomenon on the ground, increasing their safety through building awareness and understanding of the quantifiable extreme changes underway.

Data Availability Statement

All data used in this work is published at https://doi.org/10.5281/zenodo.6433389 (Castellnou et al., 2022).

Acknowledgments
This paper and its research would not have been possible without the Catalan Fire and Rescue Service (Bombers de la Generalitat de Catalunya) and especially the GRAF units. We thank Bombers for allowing us not only to gather detailed, invaluable data during really complex emergencies. We understand how unique the opportunity of this first step has been, and we are very grateful. We thank Tomas Artes and EU JRC GWIS team for his open data and discussion. We thank LIAISE field campaign in Catalonia during July 2021, especially Axel Roy and Guylaine Canut and the DESR/CNRM/GMEI/4M team, for the environmental radiosoundings datasets (https://doi.org/10.25326/322). We thank Steve Gibson, Scott Purdy, Andrea Duane, Rut Domenech, Laia Estivill, and Brian Verhoeven for their expertise and assistance throughout our study and for their feedback and discussion on an earlier version of this manuscript.

References

Abatzoglou, J. T., Williams, A. P., & Barbero, R. (2019). Global emergence of anthropogenic climate change in fire weather indices. *Geophysical Research Letters*, *46*(1), 326–336. https://doi.org/10.1029/2018GL080959

American Meteorological Society. (2021). Pyrocumulonimbus, glossary of meteorology. Retrieved from http://glossary.ametsoc.org/wiki/Pyrocumulonimbus

Anderson, H. E. (1982). Aids to determining fuel models for estimating fire behavior. In *General technical report INT-122* (p. 22). USDA Forest Service. Intermountain Forest and Range Experimental Station.

Andrews, P. L. (2009). *BehavePlus fire modeling system, version 5.0: Variables. General Technical Report RMRS-GTR-213 revised* (Vol. 111, p. 213). Department of Agriculture, Forest Service, Rocky Mountain Research Station.

Andrews, P. L. (2018). *The Rothermel surface fire spread model and associated developments: A comprehensive explanation. General Technical Report RMRS-GTR-371* (p. 121). U.S. Department of Agriculture, Forest Service, Rocky Mountain Research Station.

Andrews, P. L., Heinsch, F. A., & Schelvan, L. (2011). *How to generate and interpret fire characteristics charts for surface and crown fire behavior. General Technical Report RMRS-GTR-253* (p. 40). U.S. Department of Agriculture, Forest Service, Rocky Mountain Research Station. Retrieved from http://www.treesearch.fs.fed.us/pubs/37380

Arreola Amaya, M., & Clements, C. B. (2020). Evolution of plume core structures and turbulence during a wildland fire experiment. *Atmosphere*, *11*(8), 842. https://doi.org/10.3390/atmos11080842

Artés, T., Castellnou, M., Houston Durrant, T., & San-Miguel, J. (2022). Wildfire–atmosphere interaction index for extreme-fire behaviour. *Natural Hazards and Earth System Sciences*, *22*(2), 509–522. https://doi.org/10.5194/nhess-22-509-2022

Bakhshaii, A., Johnson, E. A., & Nayebi, K. (2020). Wildfire pyroconvection and CAPE: Buoyancy's drying and atmospheric intensification-fort McMurray. *Atmosphere*, *11*(7), 763. https://doi.org/10.3390/ATMOS11070763

Beebe, R. G. (1955). Types of air masses in which tornadoes occur. *Bulletin America Meteorology Social*, *36*, 349–350.

Bessardon, G. E. Q., Fosu-Amankwah, K., Petersson, A., & Brooks, B. J. (2019). Evaluation of Windsond S1H2 performance in Kumasi during the 2016 DACCIWA field campaign. *Atmospheric Measurement Techniques*, *12*(2), 1311–1324. https://doi.org/10.5194/amt-12-1311-2019

Biondi, R., Randel, W. J., Ho, S.-P., Neubert, T., & Syndergaard, S. (2012). Thermal structure of intense convective clouds derived from GPS radio occultations. *Atmospheric Chemistry and Physics*, *12*, 5309–5318. https://doi.org/10.5194/acp-12-5309-2012

Boone, A., Best, M., Cuxart, J., Polcher, J., Quintana, P., Bellvert, J., et al. (2019). Land surface interactions with the atmosphere over the Iberian Semi-arid Environment (LIAISE). *Gewex News*, *29*(1), 8–10.

Byram, G. M. (1959). Forest fire behavior. In K. P. Davis (Ed.), *Forest fire: Control and use* (pp. 90–123). McGraw-Hill.

Castellnou, M., Bachfischer, M., Miralles, M., Ruiz, B., Stoof, C. R., & Vilà-Guerau de Arellano, J. (2022). Pyroconvection classification based on atmospheric vertical profiling correlation with extreme fire spread observations [Dataset]. Zenodo. https://doi.org/10.5281/zenodo.6433389

Castellnou, M., Guiomar, N., Rego, F., & Fernandes, P. M. (2018). Fire growth patterns in the 2017 mega fire episode of the 15th of October, central Portugal. In D. X. Viegas (Ed.), *Advances in forest fire research 2018. Chapter 3—Fire management*. https://doi.org/10.14195/978-989-26-16-506_48

Charland, A. M., & Clements, C. (2013). Kinematic structure of a wildland fire plume observed by Doppler lidar. *Journal of Geophysical Research: Atmospheres*, *118*(8), 3200–3212. https://doi.org/10.1002/jgrd.50308

Charney, J. C., & Potter, B. E. (2017). Convection and downbursts. *Fire Management Today*, *75*(1), 16–19.

Clark, T. L., Jenkins, M. A., Coen, J. L., & Packham, D. R. (1996). A coupled atmosphere-fire model: Role of the convective Froude number and dynamic Fingering at the fireline. *International Journal of Wildland Fire*, *6*(4), 177–190. https://doi.org/10.1071/wf9960177

Clements, C. B., Lareau, N. P., Kingsmill, D. E., Bowers, C. L., Camacho, C. P., Bagley, R., & Davis, B. (2018). The rapid deployments to wildfires experiment (RaDFIRE): Observations from the fire zone. *Bulletin of the American Meteorological Society*, *99*(12), 2539–2559. https://doi.org/10.1175/bams-d-17-0230.1

Coen, J. L., Cameron, M., Michalakes, J., Patton, E. G., Riggan, P. J., & Yedinak, K. M. (2013). WRF-Fire: Coupled weather–wildland fire modeling with the weather research and forecasting model. *Journal of Applied Meteorology and Climatology*, *52*(1), 16–38. https://doi.org/10.1175/jamc-d-12-023.1

Di Virgilio, G., Evans, J. P., Blake, S. A., Armstrong, M., Dowdy, A. J., Sharples, J., & McRae, R. (2019). Climate change increases the potential for extreme wildfires. *Geophysical Research Letters*, *46*(14), 8517–8526. https://doi.org/10.1029/2019gl083699

Duane, A., Castellnou, M., & Brotons, L. (2021). Towards a comprehensive look at global drivers of novel extreme wildfire events. *Climatic Change*, *165*(3–4), 1–21. https://doi.org/10.1007/s10584-021-03066-4

Dworak, R., Bedka, K., Brunner, J., & Feltz, W. (2012). Comparison between GOES-12 2 overshooting-top detections, WSR-88D radar reflectivity, and severe storm reports. *Weather and Forecasting*, *27*(3), 684–699. https://doi.org/10.1175/waf-d-11-00070.1

Eghdami, M., Juliano, T. W., Jimenez, P., Kosovic, B., Castellnou, M., & Vilà-Guerau de Arellano, J. (2021). An idealized study of environmental variables and fire emissions impact on pyroconvective clouds with WRF-Fire. In *102nd AGU fall meeting, December 13–17, New Orleans, LA*.

EUCPM. (2017). *Situación de incendios forestales en Chile entre Enero-Febrero 2017*. European Union Civil Protection Mechanism.

Filippi, J. B., Bosseur, F., Mari, C., Lac, C., Le Moigne, P., Cuenot, B., et al. (2009). Coupled atmosphere–wildland fire modelling. *Journal of Advances in Modeling Earth Systems*, *2*, 11. https://doi.org/10.3894/james.2009.1.11

Finney, M., McAllister, S., Grumstrup, T., & Forthofer, J. (2021). *Wildland fire behavior: Dynamics, principles and processes*. CSIRO Publishing.

Finney, M. A. (1998). FARSITE: Fire area simulator-model development and evaluation. In *USDA Forest Service, Rocky Mountain Research Station Research Paper RMRS RP 4, Ogden, UT*.

Finney, M. A., Cohen, J. D., Forthofer, J. M., McAllister, S. S., Gollner, M. J., Gorham, D. J., et al. (2015). Role of buoyant flame dynamics in wildfire spread. *Proceedings of the National Academy of Sciences*, *112*(32), 9833–9838. https://doi.org/10.1073/pnas.1504498112

Fromm, M., Lindsey, D. T., Servranckx, R., Yue, G., Trickl, T., Sica, R., & Godin-Beekmann, S. (2010). The untold story of pyrocumulonimbus. *Bulletin of the American Meteorological Society*, *91*(9), 1193–1209. https://doi.org/10.1175/2010bams3004.1

Fromm, M., McRae, R. H. D., Sharples, J. J., & Kablick III, G. P. (2012). Pyrocumulonimbus pair in Wollemi and Blue Mountains National Parks, the 22nd of November 2006. *Australian Meteorological and Oceanographic Journal*, *62*(3), 117–126. https://doi.org/10.22499/2.6203.001

GENCAT. (2021). Dades Incendis. Retrieved from http://agricultura.gencat.cat/ca/ambits/medi-natural/incendis-forestals/dades-incendis/

Goens, D. W., & Andrews, P. L. (1998). Weather and fire behavior factors related to the 1990 Dude fire near Payson, Arizona. In *Proceedings of the 2nd conference on fire and forest meteorology, Phoenix, AZ*. American Meteorological Society.

González-Olabarria, J. R., Piqué, M., & Busquets, E. (2019). *Cartografia de vegetació per la simulació d'incendis forestals*. Servidor PREVINCAT.

Guerreiro, J., Fonseca, C., Salgueiro, A., Fernandes, P., Lopez, E., de Neufville, R., et al. (2017). Analise e apuramento dos factos relativos aos incˆendios que ocorreram em Pedrogao Grande, Castanheira de Pera, Ansiao, Alvaiazere, Figueiro dos Vinhos, Arganil, Gois, Penela, Pampilhosa da Serra, Oleiros e Serta entre 17 e 24 de junho de 2017 (Analysis and Fact Finding of the Wildfires Occurring in Pedrogao Grande, Castanheira de Pera, Ansiao, Alvaiazere, Figueiro dos Vinhos, Arganil, Gois, Penela, Pampilhosa da Serra, Oleiros and Serta Between 17 and 24 June 2017) Comissao Tecnica Independente. Assembleia da Republica. Governo Portugues, Lisboa. Lisboa. Portugal. (In Portuguese). Retrieved from https://www.parlamento.pt/Documents/2017/Outubro/RelatórioCTI_VF.pdf

Guerreiro, J., Fonseca, C., Salgueiro, A., Fernandes, P., Lopez Iglésias, E., de Neufville, R., et al. (2018). *Avaliaçao dos incendios ocorridos entre 14 e 16 de Outubro de 2017 em Portugal Continental [Study of the Wildfires that Occurred Between 14 and 16 October 2017 in Continental Portugal] Relatorio Final. Comissao Tecnica Independente*. Assembleia da República. (In Portuguese).

Haines, D. A. (1988). A lower atmosphere stability index for wildland fires. *National Weather Digest*, *13*, 23–27.

Harris, S., Anderson, W., Kilinc, M., & Fogarty, L. (2012). The relationship between fire behaviour measures and community loss: An exploratory analysis for developing a bushfire severity scale. *Natural Hazards*, *63*(2), 391–415. https://doi.org/10.1007/s11069-012-0156-y

Hersbach, H., Bell, B., Berrisford, P., Hirahara, S., Horányi, A., Muñoz-Sabater, J., et al. (2020). The ERA5 global reanalysis. *Quarterly Journal of the Royal Meteorological Society*, *146*(730), 1999–2049. https://doi.org/10.1002/qj.3803

Heus, T., & Jonker, H. J. J. (2008). Subsiding shells around shallow cumulus clouds. *Journal of the Atmospheric Sciences*, *65*(3), 1003–1018. https://doi.org/10.1175/2007JAS2322.1

Johnson, R. H., Schumacher, R. S., Ruppert, J. H., Jr., Lindsey, D. T., Ruthford, J. E., & Kriederman, L. (2014). The role of convective outflow in the Waldo Canyon fire. *Monthly Weather Review*, *142*(9), 3061–3080. https://doi.org/10.1175/mwr-d-13-00361.1

Jolly, W. M., Cochrane, M. A., Freeborn, P. H., Holden, Z. A., Brown, T. J., Williamson, G. J., & Bowman, D. M. J. S. (2015). Climate-induced variations in global wildfire danger from 1979 to 2013. *Nature Communications*, *6*(1), 7537. https://doi.org/10.1038/ncomms8537

Kochanski, A. K., Jenkins, M. A., Yedinak, K., Mandel, J., Beezley, J., & Lamb, B. (2015). Toward an integrated system for fire, smoke and air quality simulations. *International Journal of Wildland Fire*, *25*(5), 534–546. https://doi.org/10.1071/wf14074

Kuang, Z., & Bretherton, C. S. (2006). A mass-flux scheme view of a high-resolution simulation of a transition from shallow to deep cumulus convection. *Journal of the Atmospheric Sciences*, *63*(7), 1895–1909. https://doi.org/10.1175/JAS3723.1

Lareau, N. P., & Clements, C. B. (2016). Environmental controls on pyrocumulus and pyrocumulonimbus initiation and development. *Atmospheric Chemistry and Physics*, *16*(6), 4005–4022. https://doi.org/10.5194/acp-16-4005-2016

Lareau, N. P., & Clements, C. B. (2017). The mean and turbulent properties of a wildfire convective plume. *Journal of Applied Meteorology and Climatology*, *56*(8), 2289–2299. https://doi.org/10.1175/jamc-d-16-0384.1

Lareau, N. P., Nauslar, N. J., & Abatzoglou, J. T. (2018). The Carr Fire vortex: A case of pyrotornadogenesis? *Geophysical Research Letters*, *45*(23), 13–107. https://doi.org/10.1029/2018gl080667

Leach, R. N., & Gibson, C. V. (2021). Assessing the potential for pyroconvection and wildfire blow ups. *Journal of Operational Meteorology*, *9*, 47–61. https://doi.org/10.15191/NWAJOM.2021.0904

Liu, S., & Liang, X. Z. (2010). Observed diurnal cycle climatology of planetary boundary layer height. *Journal of Climate*, *23*(21), 5790–5809. https://doi.org/10.1175/2010JCLI3552.1

Luderer, G., Trentmann, J., & Andreae, O. M. (2009). A new look at the role of fire-released moisture on the dynamics of atmospheric pyro-convection. *International Journal of Wildland Fire*, *18*(5), 554–562. https://doi.org/10.1071/wf07035

Luderer, G., Trentmann, J., Winterrath, T., Textor, C., Herzog, M., Graf, H. F., & Andreae, M. O. (2006). Modeling of biomass smoke injection into the lower stratosphere by a large forest fire (part II): Sensitivity studies. *Atmospheric Chemistry and Physics*, *6*(12), 5261–5277. https://doi.org/10.5194/acp-6-5261-2006

May, R. M., Arms, S. C., Marsh, P., Bruning, E., Leeman, J. R., Goebbert, K., et al. (2022). *MetPy: A Python package for meteorological data*. Unidata. https://doi.org/10.5065/D6WW7G29. Retrieved from https://github.com/Unidata/MetPy

McAllister, S. (2021). Effect of reduced plume entrainment on the burning rate of porous fuel beds. *Progress in Scale Modeling an International Journal*, *2*(2), 6. https://doi.org/10.13023/psmij.2021.02-02-06

McRae, R. H. D. (2003). *The breath of the dragon-observations of the January 2003 ACT bushfires*. Emergency Services Bureau.

McRae, R. H. D., Sharples, J. J., & Fromm, M. (2015). Linking local wildfire dynamics to pyroCb development. *Natural Hazards and Earth System Sciences*, *15*(3), 417–428. https://doi.org/10.5194/nhess-15-417-2015

Moncrieff, M. W., & Miller, M. J. (1976). The dynamics and simulation of tropical cumulonimbus and squall lines. *Quarterly Journal of the Royal Meteorological Society*, *102*(432), 373–394. https://doi.org/10.1002/qj.49710243208

Morvan, D., & Frangieh, N. (2018). Wildland fires behaviour: Wind effect versus Byram's convective number and consequences upon the regime of propagation. *International Journal of Wildland Fire*, *27*(9), 636–641. https://doi.org/10.1071/wf18014

Nelson, R. M. (1993). Byram derivation of the energy criterion for forest and wildland fires. *International Journal of Wildland Fire*, *3*(3), 131–138. https://doi.org/10.1071/WF9930131

Peterson, D. A., Hyer, E. J., Campbell, J. R., Fromm, M. D., Hair, J. W., Butler, C. F., & Fenn, M. A. (2015). The 2013 Rim Fire: Implications for predicting extreme fire spread, pyroconvection, and smoke emissions. *Bulletin America Meteorology Social*, *96*(2), 229–247. https://doi.org/10.1175/BAMS-D-14-00060.1

Peterson, D. A., Hyer, E. J., Campbell, J. R., Solbrig, J. E., & Fromm, M. D. (2017). A conceptual model for development of intense pyrocumulus in western North America. *Monthly Weather Review*, *145*(6), 2235–2255. https://doi.org/10.1175/MWR-D-16-0232.1

Pino, D., de Arellano, J. V. G., & Duynkerke, P. G. (2003). The contribution of shear to the evolution of a convective boundary layer. *Journal of the Atmospheric Sciences*, *60*(16), 1913–1926. https://doi.org/10.1175/1520-0469(2003)060<1913:tcostt>2.0.co;2

Pinto, M. M., DaCamara, C. C., Hurduc, A., Trigo, R. M., & Trigo, I. F. (2020). Enhancing the fire weather index with atmospheric instability information. *Environmental Research Letters*, *15*(9), 0940b7. https://doi.org/10.1088/1748-9326/ab9e22

Potter, B. E. (2002). A dynamics based view of atmosphere-fire interactions. *International Journal of Wildland Fire*, *11*(4), 247–255. https://doi.org/10.1071/wf02008

Potter, B. E. (2005). The role of released moisture in the atmospheric dynamics associated with wildland fires. *International Journal of Wildland Fire*, *14*(1), 77–84. https://doi.org/10.1071/WF04045

Potter, B. E. (2012). Atmospheric interactions with wildland fire behaviour—II. Plume and vortex dynamics. *International Journal of Wildland Fire*, *21*(7), 802–817. https://doi.org/10.1071/wf11129

Potter, B. E., & Hernandez, J. R. (2017). Downdraft outflows: Climatological potential to influence fire behaviour. *International Journal of Wildland Fire*, *26*(8), 685–692. https://doi.org/10.1071/WF17035

PREVINCAT. (2021). PREVINCAT server. Retrieved from https://previncat.ctfc.cat/

Pyne, S. J. (2019). *Fire: A brief history*. University of Washington Press.

Richardson, H., Basu, S., & Holtslag, A. A. M. (2013). Improving stable boundary-layer height estimation using a stability-dependent critical bulk Richardson number. *Boundary-Layer Meteorology*, *148*(1), 93–109. https://doi.org/10.1007/s10546-013-9812-3

Rodts, S. M. A., Duynkerke, P. G., & Jonker, H. J. J. (2003). Size distributions and dynamical properties of shallow cumulus clouds from aircraft observations and satellite data. *Journal of the Atmospheric Sciences*, *60*(16), 1895–1912. https://doi.org/10.1175/1520-0469(2003)060<1895:sdadpo>2.0.co;2

Rothermel, R. C. (1972). *A mathematical model for predicting fire spread in wildland fuels* (Vol. 115). Intermountain Forest and Range Experiment Station, Forest Service.

Rothermel, R. C. (1991). *Predicting behavior and size of crown fires in the northern Rocky Mountains Research Paper INT-438*. U.S. Department of Agriculture, Forest Service, Intermountain Research Station 46. https://doi.org/10.2737/INT-RP-438

Ruffault, J., Curt, T., Martin-St Paul, N. K., Moron, V., & Trigo, R. M. (2018). Extreme wildfire events are linked to global-change-type droughts in the northern Mediterranean. *Natural Hazards and Earth System Sciences*, *18*(3), 847–856. https://doi.org/10.5194/nhess-18-847-2018

San-Miguel-Ayanz, J., Oom, D., Artes, T., Viegas, D., Fernandes, P., Faivre, N., et al. (2020). Forest fires in Portugal in 2017. In A. Casajus Valles (Ed.), *Science for Disaster risk Management 2020: Acting today, protecting tomorrow*.

Servei Català de Meteorologia. (2021). Retrieved from https://www.meteo.cat/

Stull, R. B. (1988). *An introduction to boundary layer meteorology* (p. 666). Kluwer Academic.

Tedim, F., Leone, V., Amraoui, M., Bouillon, C., Coughlan, M. R., Delogu, G. M., et al. (2018). Defining extreme wildfire events: Difficulties, challenges, and impacts. *Fire*, *1*(1), 1–28. https://doi.org/10.3390/fire1010009

Thunis, P., Rouil, L., Cuvelier, C., Stern, R., Kerschbaumer, A., Bessagnet, B., et al. (2007). Analysis of model responses to emission-reduction scenarios within the CityDelta project. *Atmospheric Environment*, *41*(1), 208–220. https://doi.org/10.1016/j.atmosenv.2006.09.001

Tory, K. J., & Kepert, J. D. (2020). Pyrocumulonimbus firepower threshold: Assessing the atmospheric potential for PyroCb. *Weather and Forecasting*, *36*(2), 439–456. https://doi.org/10.1175/waf-d-20-0027.1

Tory, K. J., Thurston, W., & Kepert, J. D. (2018). Thermodynamics of pyrocumulus: A conceptual study. *Monthly Weather Review*, *146*(8), 2579–2598. https://doi.org/10.1175/MWR-D-17-0377.1

Troen, I., & Mahrt, L. (1986). A simple model of the planetary boundary layer: Sensitivity to surface evaporation. *Boundary-Layer Meteorology*, *37*(1–2), 129–148. https://doi.org/10.1007/bf00122760

Turco, M., Rosa-Cánovas, J. J., Bedia, J., Jerez, S., Montávez, J. P., Llasat, M. C., & Provenzale, A. (2018). Exacerbated fires in Mediterranean Europe due to anthropogenic warming projected with non-stationary climate-fire models. *Nature Communications*, *9*(1), 3821. https://doi.org/10.1038/s41467-018-06358-z

Van Heerwaarden, C. C., Vilà-Guerau de Arellano, J., Moene, A. F., & Holstag, A. M. (2009). Interactions between dry-air entrainment, surface evaporation and convective boundary-layer development. *Quarterly Journal of the Royal Meteorological Society*, *135*(642), 1277–1291. https://doi.org/10.1002/qj.431

Van Wagner, C., & Forest, P. (1987). Development and structure of the Canadian forest fire weather index system. In *Canadian Forestry Service, Forest Technical Report*.

Vilà-Guerau de Arellano, J., Van Heerwaarden, C. C., Van Stratum, B. J., & Van Den Dries, K. (2015). Atmospheric boundary layer: Integrating air chemistry and land interactions.

Vogelezang, D. H. P., & Holtslag, A. A. M. (1996). Evaluation and model impacts of alternative boundary-layer height formulations. *Boundary-Layer Meteorology*, *81*(3–4), 245–269. https://doi.org/10.1007/BF02430331

Wakimoto, R. M. (1985). Forecasting dry microburst activity over the high plains. *Monthly Weather Review*, *113*(7), 1131–1143. https://doi.org/10.1175/1520-0493(1985)

Werth, P. A., Potter, B. E., Alexander, M. E., Clements, C. B., Cruz, M. G., Finney, M. A., et al. (2016). Synthesis of knowledge of extreme fire behavior: Volume 2 for fire behavior specialists, researchers, and meteorologists. In *General Technical Report PNW-GTR-891* (p. 258). U.S. Department of Agriculture, Forest Service, Pacific Northwest Research Station.

WMO. (2017). International cloud Atlas.

Zhang, Y., Gao, Z., Li, D., Li, Y., Zhang, N., Zhao, X., & Chen, J. (2014). On the computation of planetary boundary-layer height using the bulk Richardson number method. *Geoscientific Model Development*, *7*(6), 2599–2611. https://doi.org/10.5194/gmd-7-2599-2014